

A unified kinematic wave theory for melt infiltration into firn

Mohammad Afzal Shadab^{1,2,3}, Anja Rutishauser⁴, Cyril Grima², Marc Andre Hesse^{1,5}

¹ *Oden Institute for Computational Engineering and Sciences, University of Texas at Austin, USA*

² *University of Texas Institute for Geophysics, The University of Texas at Austin, USA*

³ *Department of Civil and Environmental Engineering, Princeton University, USA*

⁴ *Department of Glaciology and Climate, Geological Survey of Denmark and Greenland, Denmark*

⁵ *Department of Earth and Planetary Sciences, Jackson School of Geosciences, University of Texas at Austin, USA*

Correspondence: Mohammad Afzal Shadab <mashadab@princeton.edu>

ABSTRACT. Motivated by the ponding refreezing of meltwater in firn, we analyze the interaction of liquid water and non-reactive gas with porous ice by developing a unified kinematic wave theory. The wave theory is based on the conservation of composition and enthalpy, coupling advective heat and mass transport in firn, and encompasses cases of meltwater perching where the conventional kinematic wave approximation fails. For simple initial conditions (Riemann problems), this model allows for self-similar solutions that reveal the structure of melting/refreezing fronts, with analytical solutions provided for 12 basic cases of physical relevance encountered in the literature. These solutions offer insights into processes such as the formation of frozen fringes, the perching of meltwater on low porosity layers, and conditions for impermeable ice layer formation. This theoretical framework can enhance our understanding of the partitioning between meltwater infiltration and surface runoff, which influences surface mass loss from ice sheets and contributes to sea level rise. Furthermore, these analytic solutions serve as benchmarks for numerical models, and can aid in the improvement and comparison of firn hydrology, ice-sheet, and Earth system models.

1 INTRODUCTION

Large fractions of the Greenland and Antarctic ice sheets are covered in porous firn (Verjans and others, 2021; Noël and others, 2022). Increasingly, this firn is experiencing periods of surface melting and even rainfall and infiltration of (melt) water (Van Angelen and others, 2013; Bell and others, 2018; Harper and others, 2023). Refreezing of this melt within the firn has the capacity to absorb a significant fraction of this water and prevent mass loss to the ocean (Harper and others, 2012; Van Angelen and others, 2013; de la Peña and others, 2015). However, the increasing frequency of infiltration events had led to a rapid increase in large-scale ice layers within the firn that may buffer its water storage capacity, leading to increased lateral water flow and eventually mass loss from the ice sheet to the ocean (Pfeffer and others, 1991; Van Angelen and others, 2013; Noël and others, 2017). Additionally, significant amounts of liquid water are stored in firn aquifers, which heat the surrounding firn and delay meltwater runoff (Forster and others, 2014; Amory and others, 2024). The critical role of firn in modulating melt runoff has led to increased interest in flow and transport processes in wet firn or firn hydrology (Amory and others, 2024).

Of particular interest is the formation of ice layers which requires the localization of freezing in a narrow vertical interval within the firn. Localization can either occur by ponding of melt on pre-existing discontinuities within the firn (Marsh and Woo, 1984; Pfeffer and Humphrey, 1998; Wever and others, 2016; Humphrey and others, 2021a) or due to the rapid arrest of the wetting front after a melting event as the liquid water content declines and conduction becomes dominant to freeze melt in place (Shadab and others, 2024a). Impermeable ice layers likely form gradually and require multiple refreezing events to reduce porosity below the pore close-off. As the permeability of the ice layer decreases, melt percolation slows sufficiently for the infiltrating melt to pond and form a perched aquifer that spreads laterally. Within the perched aquifer the melt will fully saturate the firn. To understand the evolution of ice layers and aquifers, it is therefore important to understand the interaction of melt with layers of lower permeability, the transition from unsaturated to saturated flow and the conditions that reduce ice layer permeability to zero. Currently there is no physics-based model that can describe the formation of an ice layer with zero permeability (hereafter referred to as an impermeable ice layer). Here we aim to develop a first-order model that captures this process, based on a theoretical framework for the coupling of energy and mass transport in firn.

1.1 Modeling melt infiltration into firn

Modeling the infiltration of water from both rainfall and surface melting into firn is still a challenging problem and model predictions diverge due to different approaches to representing melt percolation in firn and poorly characterised constitutive relations (Stevens and others, 2020; Vandecrux and others, 2020; Amory and others, 2024). Models for firn hydrology must include both mass and energy transport and incorporate both the non-linearity inherent in unsaturated flow in porous media and the non-linearity of the phase change during freezing and melting.

The most commonly used approach to unsaturated flow in firn, so-called bucket models, combine mass conservation with a discrete percolation model, based on the concept that the melt needs to reach a maximum holding capacity or irreducible water content before it advances to the next layer of the firn (Coléou and Lesaffre, 1998; Bartelt and Lehning, 2002; Ligtenberg and others, 2011; Kuipers Munneke and others, 2015; Vionnet and others, 2012; Verjans and others, 2019). A second approach combines mass balance with the two-phase extension of Darcy's law to obtain a kinematic wave model (Colbeck, 1974a; Jordan, 1991; Singh, 1997; Clark and others, 2017; Shadab and others, 2024a). This approach can be extended to include the effects of capillary suction leading to Richards' equation (Illangasekare and others, 1990; Wever and others, 2014; Meyer and Hewitt, 2017). More complex and multi-dimensional models have been developed to capture the process of preferential flow and ice pipe formation in snow and firn (Marsh and Woo, 1984; Schneebeli, 1995; Katsushima and others, 2013). These models build upon Richards' equation by extending it to include either an imbibition water entry pressure (Hirashima and others, 2014; Leroux and Pomeroy, 2017), a dynamic capillary pressure (Hassanizadeh and others, 2002; Leroux and Pomeroy, 2019) or apparent surface tension at the wetting front (Cueto-Felgueroso and Juanes, 2008; Moure and others, 2023).

Similarly, phase change and the associated latent heat is handled with different approaches in firn hydrology. Most models assume thermal equilibrium between melt and ice and the main difficulty in treating the phase change is that temperature is not an independent variable at the melting point (Anderson and Crerar, 1993). Percolation or bucket models are inherently discrete and handle the phase change with a discrete algorithm comparing the heat content of the melt with the cold content of the firn layer (Bartelt and Lehning, 2002; Ligtenberg and others, 2011; Kuipers Munneke and others, 2015). Darcy models treat phase change either discretely (Illangasekare and others, 1990), avoid the degeneracy by distributing the phase change over a finite temperature interval (Clark and others, 2017), employ the enthalpy method

(Jordan, 1991; Meyer and Hewitt, 2017; Shadab and others, 2024a), or allow for thermal disequilibrium (Moure and others, 2023; Jones and others, 2024).

The coupling between energy and mass transport and the inherent non-linearities of both unsaturated flow and phase change, together with the different modeling strategies summarized above lead to wide discrepancies between predictions of different firn models (Vandecrux and others, 2020). Improving these models therefore requires a comprehensive and systematic evaluation strategy (Clark and others, 2017). Analytic solutions to synthetic test cases are an important element of model evaluation because they allow evaluation of numerical implementation, such as the discretization and coupling strategies. In this context, kinematic wave models are useful for firn hydrology because they contain both the essential non-linearities of unsaturated flow and phase change as well as the coupling between mass and energy transport, yet they allow for analytical solutions for simple initial conditions. Past work on kinematic waves has been restricted to unsaturated conditions, but understanding the formation of impermeable ice layers that lead to ponding and the formation of saturated regions is crucial for estimating meltwater runoff versus storage in firn. Shadab and Hesse (2022) have shown that these saturated regions can be included in an extended kinematic theory that allows us to investigate these processes. The purpose of this paper is to derive a set of self-similar analytic solutions and to determine the conditions that lead to the formation of impermeable ice layers and perched aquifers.

1.2 Kinematic wave theory for firn hydrology

Due to the large porosity and grain size of firn, the vertical flow of water may be primarily governed by gravity, while capillary suction/diffusion may play a minor role (Colbeck, 1972, 1974b). Neglecting capillary diffusion results in a non-linear kinematic wave model that describes the evolution of the water/melt saturation in the firn (Colbeck, 1972). Kinematic wave theory is a framework used to describe the propagation of waves in systems where the wave motion is influenced primarily by the kinematics, or the motion of particles, rather than by the dynamics or forces acting on them (Lighthill and Whitham, 1955). In case of melt infiltration, the kinematic wave model results in a hyperbolic partial differential equation that allows analytic solutions in one dimension using the method of characteristics (MOC) (Lighthill and Whitham, 1955; LeVeque, 1992). These analytic solutions describe non-linear waves, e.g., wetting and drying fronts, and their interaction which capture the main features of field observations, for example from melt infiltration in the Seward glacier firn on the St. Elias mountains in Canada (Sharp, 1951).

Initial work on kinematic models for melt migration focused on temperate snow where phase change is not important and unsaturated flow models could be adapted directly (Colbeck, 1971, 1972; Colbeck and Davidson, 1973). Later, Colbeck (1976) added thermodynamics to the kinematic theory to study infiltration into cold firn that requires refreezing of the melt at the wetting front. He shows that the retardation of the wetting front is relatively minor in snow because the latent heat of fusion is large. This model has been applied to analyze the effects of an impermeable basal boundary (Colbeck, 1974a), the retention of water in snow (Colbeck, 1976) and the effects of layering and heterogeneity (Colbeck, 1979, 1991). The theory has also been used to estimate the permeability of snow using lysimeter data (Colbeck and Anderson, 1982). Singh and others (1997) and Clark and others (2017) use kinematic theory to study the interaction of drying and wetting fronts which was recently identified as key to the initiation of ice layer formation (Shadab and others, 2024a). Singh and others (1997) also investigate the effect of temporal variability in rainfall rate (for review see also Singh, 1997).

1.3 Contribution of this manuscript

To understand the formation of impermeable ice layers it is important to model variably saturated flows, i.e., flows that transition from unsaturated to saturated and vice versa. The conventional kinematic wave theory for infiltration fails in a fully saturated region because the flow of water becomes pressure driven rather than gravity driven and thus, the model equations are not valid anymore (see Shadab and Hesse (2022)). Therefore, the kinematic wave theory needs an extension to capture fully saturated regions. Recently, Shadab and Hesse (2022) showed that saturated regions can be incorporated into an extended kinematic theory for simple problems, such as a step change in firn porosity. This allows the analysis of a rising perched water table, a pre-requisite for the formation of impermeable ice layers.

To address the dynamics of ice layer formation and to provide additional analytic solutions for the evaluation of the models in firn hydrology this manuscript makes the following contributions:

- Formulate coupled mass and energy transport as a system of non-linear hyperbolic conservation equations and analyze their coupling.
- Use method of characteristics to develop a set of self-similar analytic solutions for problems with an initial step change in volume fractions of ice or water (Riemann problems).
- Apply unified kinematic wave theory to firn hydrology to describe the formation of perched aquifers and derive conditions for impermeable ice layer formation.

We call it a *unified* theory, as it is not derived from prior kinematic wave theories for melt infiltration, but it still unifies most previous work and includes extensions to perched aquifers. The remainder of this paper is divided into four sections. Section 2 presents the model formulation. Section 3 considers the problem of melt transport across a discontinuity and documents twelve nature-inspired cases with their analytical solutions. Section 4.1 applies this theory to study a multilayered firn leading to formation of a perched firn aquifer and validates it with the numerical solution. Finally, Section 5 concludes the paper.

2 CONTINUUM MODEL FORMULATION

In this section, we first define the conserved quantities, then introduce the governing equations and constitutive models, and finally provide the resulting dimensionless continuum model. The related assumptions will be introduced in this work when required.

2.1 Conserved Quantities

We model firn as a three phase system comprising liquid water (w), ice (i) and gas (g). These three phases are composed of two components, namely, water (H_2O) and air (\sim Nitrogen gas, N_2). The water component partitions into the liquid and ice while the air component is confined to the gas phase. The first conserved variable is the water (H_2O) composition (kg/m^3), C , defined as the total mass of water component per unit representative elemental volume (REV) as

$$C = \rho_i \phi_i + \rho_w \phi_w. \quad (1)$$

where ρ_α is the density (kg/m^3), ϕ_α refers to volume fraction of the phase $\alpha \in \{w, i, g\}$. The formulation assumes that the water vapor component is negligible in the gas phase and that ice and water phases are pure. Assuming same density for ice and water, $\rho_i \approx \rho_w = \rho$, and the volume fraction constraint, $\phi_i + \phi_w + \phi_g = 1$, Equation (1) further simplifies to

$$C = \rho(\phi_i + \phi_w) = \rho(1 - \phi_g). \quad (2)$$

The second conserved variable is related to the thermodynamics of the system. Since phase change is involved when ice melts, temperature does not accurately represent all states of the system considered (Jordan, 1991; Alexiades and Solomon, 1993; Aschwanden and others, 2012; Carnahan and others, 2021). Therefore the second conserved variable is chosen to be the enthalpy of the system (J/m^3), H , which is defined as

$$H := \rho_i \phi_i h_i(T) + \rho_w \phi_w h_w(T) + \rho_g \phi_g h_g(T), \quad (3)$$

where h_α is the specific enthalpy (J/kg) of the phase α , which is a piecewise linear function of temperature (K), T . For simplicity we fix the reference enthalpy at the solidus to be $H = 0$ where the system is at the melting temperature, $T = T_m$. The specific enthalpy h_α of each phase $\alpha \in \{w, i, g\}$ can then be defined as

$$h_i(T) = \begin{cases} c_{p,i}(T - T_m), & T < T_m \quad (\text{or } H < 0) \\ 0, & T \geq T_m \quad (\text{or } H \geq 0) \end{cases}, \quad (4)$$

$$h_w(T) = \begin{cases} 0, & T < T_m \quad (\text{or } H < 0) \\ c_{p,w}(T - T_m) + L, & T \geq T_m \quad (\text{or } H \geq 0) \end{cases}, \quad (5)$$

$$h_g(T) = c_{p,g}(T - T_m). \quad (6)$$

Here $c_{p,\alpha}$ is the specific heat capacity at constant pressure ($\text{J/kg}\cdot\text{K}$) for phase α , T_m is the melting temperature (K) and L is the latent heat of fusion of water (J/kg). The density and specific heat capacity of gas are much lower than those of liquid water or ice, i.e., $\rho_g \ll \rho$ and $c_{p,g} < c_{p,i}$ or $c_{p,w}$ (see Table 1). Hence, we make the simplification that the gas phase contribution to the total enthalpy of the system is negligible. After substituting Equations (4) and (5) into Equation (3), H can be ultimately formulated as

$$H = \begin{cases} \rho c_{p,i} \phi_i (T - T_m), & T < T_m \quad (\text{or } H \leq 0) \\ \rho \phi_w L, & T = T_m \quad (\text{or } 0 < H < CL) \\ \rho \phi_w (c_{p,w}(T - T_m) + L), & T > T_m \quad (\text{or } H \geq CL) \end{cases}. \quad (7)$$

Here the maximum enthalpy limit for the three-phase region is the product of composition, C , and the latent heat of fusion, L because it is the enthalpy of the fully molten system at the melting point (see Figure 1a). The boundaries of the three-phase region are not included in the region $0 < H < CL$ because it strictly refers to the three phase region. From the above formulation we classify three regions, where region 1 ($H \leq 0$) is comprised of ice and gas, region 2 ($0 < H < CL$) contains all three phases and region 3 ($H \geq CL$) corresponds to a no-matrix state consisting of only water and gas phases.

The temperature and volume fractions of water, ice and gas phases can be evaluated from composition, C , and enthalpy, H , as shown in Figures 1a-1d respectively. As shown in Equation (2), the volume fraction of gas, ϕ_g , only depends on the composition, C , as shown in Figure 1d. Next we formulate the governing equations for this model corresponding to the two conserved variables.

2.2 Transport Model

In a reference frame moving with ice, the conservation equations for water composition and system enthalpy are respectively given as

$$\frac{\partial C}{\partial t} + \nabla \cdot (\mathbf{q}\rho) = 0 \quad (8)$$

$$\frac{\partial H}{\partial t} + \nabla \cdot (\mathbf{q}\rho h_w - \bar{\kappa}\nabla T) = 0, \quad (9)$$

where \mathbf{q} is the volumetric flux of water phase ($\text{m}^3/\text{m}^2\cdot\text{s}$) relative to ice phase. The effective thermal conductivity of the mixture $\bar{\kappa}$, typically a weighted average of the thermal conductivities of the phases, κ_α ($\text{W}/\text{m}\cdot\text{K}$).

2.3 Constitutive Relations

The volumetric flux of water relative to ice, \mathbf{q} , can be written using extended Darcy's law,

$$\mathbf{q} = -\frac{k(\varphi)k_{rw}(s)}{\mu}(\nabla p - \rho\mathbf{g}) \quad (10)$$

where k is the absolute permeability (m^2) which is a function of porosity φ ($\varphi = \phi_w + \phi_g = 1 - \phi_i$), the ratio of void volume to the bulk volume, p is water pressure (Pa), μ is the viscosity of water ($\text{Pa}\cdot\text{s}$) and \mathbf{g} is

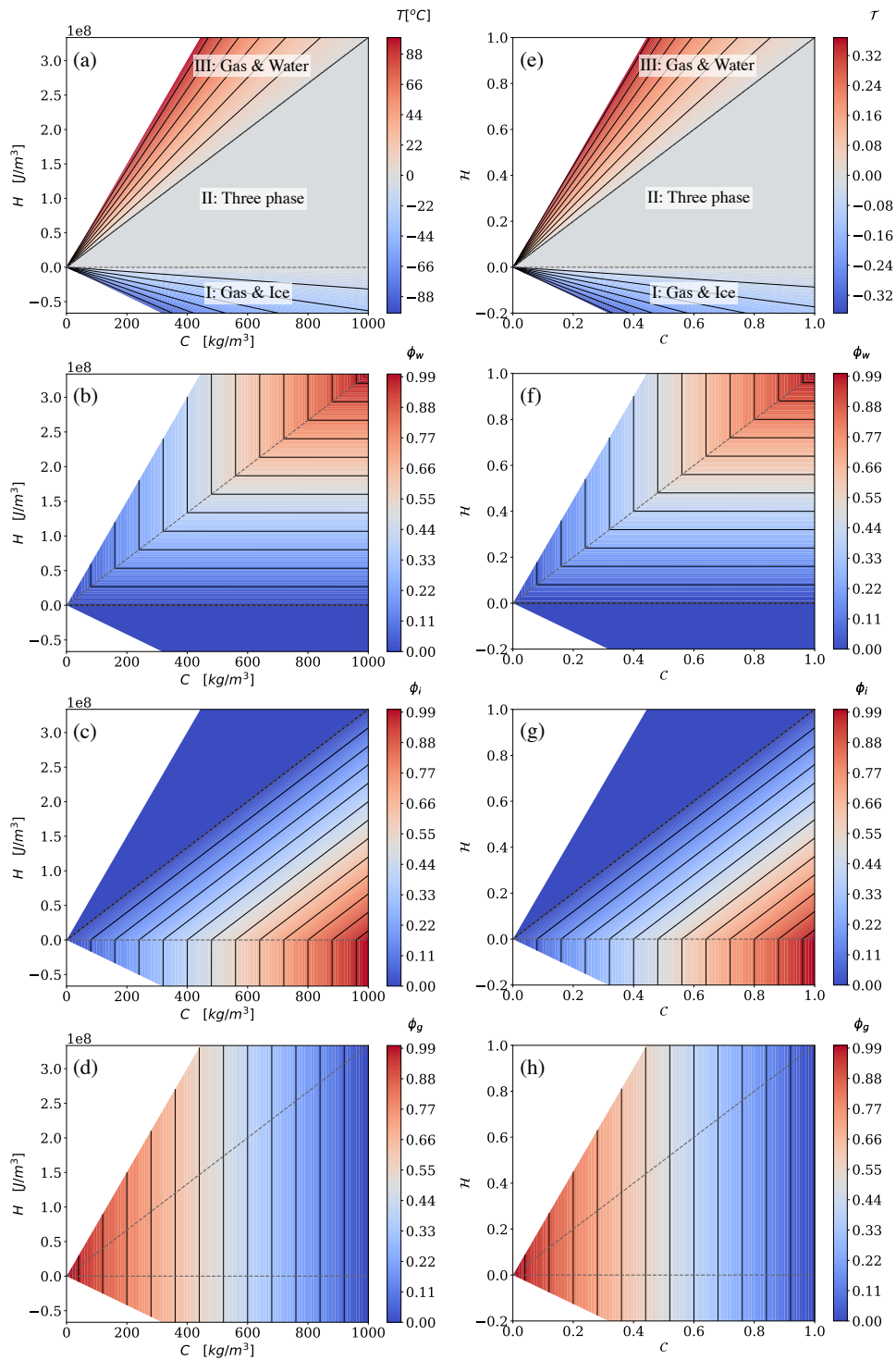


Fig. 1. The dependence of temperature and volume fractions on dimensional and dimensionless enthalpy and composition, (C, H) and $(\mathcal{C}, \mathcal{H})$ respectively. Dimensional C, H : (a) temperature and volume fractions of (b) water, (c) ice and (d) gas phases. Dimensionless \mathcal{C}, \mathcal{H} : (e) scaled temperature and volume fractions of (f) water, (g) ice and (h) gas phases. The contours are restricted to $T \in [-100^\circ\text{C}, 100^\circ\text{C}]$ to avoid phase change at boiling as well as keep the contour levels consistent. Solid black lines are the level-sets whereas the dashed lines show the boundaries of the regions, i.e., $H = 0$ or $\mathcal{H} = 0$ and $H = CL$ or $\mathcal{H} = \mathcal{C}$. The three regions are labeled in panels *a* and *e*.

the acceleration due to gravity vector (m^2/s). The relative permeability for multi-phase flow, k_{rw} , display complex hysteresis (Blunt, 2017), but here we only consider the simplest case with power law dependence. The relative permeability of the water phase, k_{rw} , is a function of the water saturation, s , which is the ratio of water phase volume to void volume, $s = \phi_w/1 - \phi_i$. We assume that the water phase becomes immobile below a certain residual water saturation, s_{wr} . Similarly the gas phase becomes immobile below the residual gas saturation, s_{gr} . As a result, the two-phase fluid flow of both gas and water phases is restricted to regions where $s_{wr} < s < 1 - s_{gr}$. We will refer to regions with $s = 1 - s_{gr}$ as saturated in the remainder of this paper. The residual water saturation during drainage has been determined to be $s_{wr} \sim 0.07$ from lysimeter (Colbeck, 1976) and calorimeter (Coléou and Lesaffre, 1998) techniques. However, as the ice is water-wet with a near-zero contact angle at the ice-water-air interface (Knight, 1971), the residual water saturation during saturation rise (imbibition) is zero due to hysteresis in the relative permeability-capillary pressure curve (Carlson, 1981; Blunt, 2017). The phenomenon of hysteresis has largely been neglected in the firn hydrology literature but it will affect the speeds of the meltwater fronts.

Next we assume the problem is gravity dominated in unsaturated regions (Colbeck, 1972), such that the spatial variations in the difference between the water and air pressure (capillary pressure) are negligible at the problem length scales. See Smith (1983); Shadab and Hesse (2022, 2024) for a more detailed discussion on neglecting the capillary pressure term in context of soils using scaling analysis. As a result, the pressure of the water phase in the unsaturated regions becomes a constant, equal to the reference gas pressure, i.e., $p = 0$ (Colbeck, 1972; Shadab and Hesse, 2022). Plugging it in Equation (10) eliminates the diffusive, pressure term. The volumetric flux of water, \mathbf{q} , finally takes the gravity-driven form

$$\mathbf{q} = \frac{k(\varphi)k_{rw}(s)}{\mu}\rho\mathbf{g}. \quad (11)$$

The absolute permeability of ice (m^2), k , and the relative permeability of water, k_{rw} , are assumed to be power laws (Kozeny, 1927; Carman, 1937; Brooks and Corey, 1964; Bear, 2013; Meyer and Hewitt, 2017) defined as

$$k(\varphi) = k_0\varphi^m = k_0(1 - \phi_i)^m, \tag{12}$$

$$k_{rw}(s) = k_{rw}^0 s^n = k_{rw}^0 \left(\frac{\phi_w}{1 - \phi_i} \right)^n, \tag{13}$$

where k_0 is a model constant, which can be considered as an absolute permeability (m^2) when there no ice matrix, and k_{rw}^0 is end point relative permeability of water phase. Here we have also assumed that the residual saturations of both water and gas phases are zero, i.e., $s_{wr} = s_{gr} = 0$. It will provide accurate speeds for the wetting fronts moving into dry firn, due to hysteresis in the relative permeability. Plugging Equations (12) and (13) in Equation (11) finally gives

$$\mathbf{q}(\phi_i, \phi_w) = \begin{cases} \mathbf{0}, & H \leq 0 \\ \frac{k_0 k_{rw}^0}{\mu} \rho g (1 - \phi_i)^m \left(\frac{\phi_w}{1 - \phi_i} \right)^n \hat{\mathbf{g}} = K_h (1 - \phi_i)^m \left(\frac{\phi_w}{1 - \phi_i} \right)^n \hat{\mathbf{g}}, & 0 < H < CL \ \& \ C < \rho \end{cases} \tag{14}$$

where the acceleration due to gravity vector is $\mathbf{g} = g\hat{\mathbf{g}}$ with $\hat{\mathbf{g}}$ being the unit vector in the direction of gravity. The symbol $K_h = \frac{k_0 k_{rw}^0}{\mu} \rho g$ is a known constant which can be considered as the maximum gravity-dependent volumetric flux of water, $|\mathbf{q}|$, at unity porosity. Note that the dynamics at unity porosity is not Darcy-type as the constitutive relationships (10-12) are only valid for a porous medium. Therefore we will restrict our analysis to the porous media where $\varphi < 1$ and the flow is laminar, thus, Darcy’s law is applicable (Tek, 1957).

2.4 Scaling

We non-dimensionalize the model to make it scale-independent and find dominant terms governing the physics of the problem. The model is scaled using dimensionless variables for composition, \mathcal{C} , enthalpy, \mathcal{H} , temperature, \mathcal{T} , depth, ζ , and time, τ , which are defined as

$$\mathcal{C} = \frac{C}{\rho}, \mathcal{H} = \frac{H}{\rho L}, \mathcal{T} = \frac{T - T_m}{T_m}, \zeta = \frac{z}{\delta}, \text{ and } \tau = \frac{t K_h}{\delta}. \tag{15}$$

Here the spatial coordinates (for example, the depth coordinate z) are non-dimensionalized by length scale of heterogeneity or the REV scale of the problem, δ . Time variable is scaled by the shortest time of water seepage across the characteristic length through a medium with unity porosity, i.e., δ/K_h . The definitions

of conserved quantities C and H , given in Equations (2) and (7) respectively, thus transform into the dimensionless forms

$$C = \phi_i + \phi_w = 1 - \phi_g, \tag{16}$$

$$\mathcal{H} = \begin{cases} C \text{Ste} \epsilon_{p,r} \mathcal{T}, & \mathcal{H} \leq 0 \\ \phi_w, & 0 < \mathcal{H} < C, \\ C(\text{Ste} \mathcal{T} + 1), & \mathcal{H} \geq C \end{cases} \tag{17}$$

where Ste is the Stefan number defined as ratio of sensible heat of water at melting temperature to the latent heat of fusion of H₂O, i.e., $\text{Ste} = c_{p,w} T_m / L$ and $\epsilon_{p,r} = c_{p,i} / c_{p,w}$ is the ratio of specific heat of ice to that of water. From the formulations of dimensionless enthalpy (17) and dimensional specific enthalpy of water phase (5), the dimensionless temperature, \mathcal{T} , and dimensionless specific enthalpy of water phase, $\mathfrak{h}_w = h_w / L$, can be derived as

$$\mathcal{T}(C, \mathcal{H}) = \begin{cases} \frac{\mathcal{H}}{C \text{Ste} \epsilon_{p,r}}, & \mathcal{H} \leq 0 \\ 0, & 0 < \mathcal{H} < C, \\ \frac{1}{\text{Ste}} \left(\frac{\mathcal{H}}{C} - 1 \right), & \mathcal{H} \geq C \end{cases} \quad \text{and} \quad \mathfrak{h}_w(C, \mathcal{H}) = \begin{cases} 0, & \mathcal{H} \leq 0 \\ 1, & 0 < \mathcal{H} < C. \\ \frac{\mathcal{H}}{C}, & \mathcal{H} \geq C \end{cases} \tag{18}$$

Subsequently the volume fractions of the phases, ϕ_α , and the porosity of the medium, φ , can be rewritten as functions of C and \mathcal{H} as

$$\phi_w(\mathcal{C}, \mathcal{H}) = \begin{cases} 0, & \mathcal{H} \leq 0 \\ \mathcal{H}, & 0 < \mathcal{H} < \mathcal{C} \\ \mathcal{C}, & \mathcal{H} \geq \mathcal{C} \end{cases}, \quad \phi_i(\mathcal{C}, \mathcal{H}) = \begin{cases} \mathcal{C}, & \mathcal{H} \leq 0 \\ \mathcal{C} - \mathcal{H}, & 0 < \mathcal{H} < \mathcal{C} \\ 0, & \mathcal{H} \geq \mathcal{C} \end{cases}, \quad (19)$$

$$\phi_g(\mathcal{C}) = 1 - \mathcal{C} \quad \text{and} \quad \varphi(\mathcal{C}, \mathcal{H}) = \begin{cases} 1 - \mathcal{C}, & \mathcal{H} \leq 0 \\ 1 - \mathcal{C} + \mathcal{H}, & 0 < \mathcal{H} < \mathcal{C} \\ 1, & \mathcal{H} \geq \mathcal{C} \end{cases}. \quad (20)$$

The scaled temperature and volume fractions of water, ice and gas phases can be evaluated from dimensionless composition, \mathcal{C} , and dimensionless enthalpy, \mathcal{H} , as shown in Figures 1e-1h respectively. As shown in Equation (2), the volume fraction of gas, ϕ_g , only depends on the dimensionless composition as illustrated in Figure 1h.

The composition and enthalpy transport equations (8 and 9) thus take the dimensionless form

$$\frac{\partial \mathcal{C}}{\partial \tau} + \nabla \cdot \left((1 - \phi_i)^m \left(\frac{\phi_w}{1 - \phi_i} \right)^n \hat{\mathbf{g}} \right) = 0, \quad (21)$$

$$\frac{\partial \mathcal{H}}{\partial \tau} + \nabla \cdot \left(\eta_w (1 - \phi_i)^m \left(\frac{\phi_w}{1 - \phi_i} \right)^n \hat{\mathbf{g}} - \frac{\bar{\kappa}}{\kappa_w} \frac{\text{Ste}}{Pe_{\mathcal{H}}} \nabla \mathcal{T} \right) = 0. \quad (22)$$

Here κ_w is the thermal conductivity of the water phase. The ratio of heat convected to heat diffused is defined as the Peclet number for enthalpy equation, $Pe_{\mathcal{H}} = K_h \delta / \alpha_T$, where $\alpha_T = \kappa_w / \rho c_{p,w}$ (m^2/s) is the thermal diffusivity of water. Moreover, the divergence and gradient operators are now scaled with inverse of characteristic depth, $1/\delta$.

While both conduction and advection can be important heat transport processes in firn (Shadab and others, 2024a), conduction does not affect the steady propagation of wetting and drying fronts analyzed here. This can be shown using thermodynamic and fluid flow parameters from Table 1. The value of Peclet number, $Pe_{\mathcal{H}}$, comes out to be $4 \cdot 10^3$ for $\delta = 1$ m. The ratio $\bar{\kappa}/\kappa_w \leq 1$ as its maximum value of unity is achieved when the REV only contains liquid water. The Stefan number Ste is a constant of value 3.43. Therefore, the value of $\frac{\bar{\kappa}}{\kappa_w} \frac{\text{Ste}}{Pe_{\mathcal{H}}}$ indicates about three orders of magnitude higher heat advection compared to heat conduction for gravity-driven infiltration in firn. Therefore, we can neglect the second

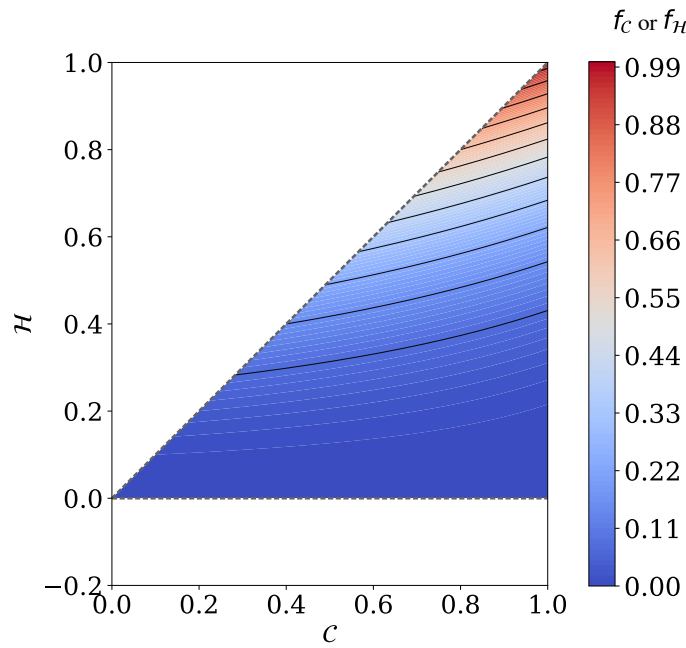


Fig. 2. The dimensionless flux of composition or enthalpy in \mathcal{CH} phase space for $m = 3$ and $n = 2$. In region 1 consisting of water and gas region ($\mathcal{H} \leq 0$) as well as region 3 comprising of three phase region ($0 < \mathcal{H} < \mathcal{C}$), the flux of dimensionless enthalpy and composition are identical, i.e., $f_C = f_H$. Region 3 with water and gas ($\mathcal{H} \geq \mathcal{C}$) is not considered in the present work.

order heat conduction term in Equation (22), which is also the necessary condition in the three phase region ($0 < \mathcal{H} < \mathcal{C}$ or $\mathcal{T} = 0$) as $\nabla \mathcal{T} = 0$. Assuming local thermodynamic equilibrium, in the limit $Pe_{\mathcal{H}} \rightarrow \infty$, the system of dimensionless governing equations (21 and 22) then reduces to quasi-linear system of coupled hyperbolic equations,

$$\frac{\partial \mathbf{u}}{\partial \tau} + \nabla \cdot \mathbf{f}(\mathbf{u}) = \mathbf{0} \tag{23}$$

where $\mathbf{u} = [\mathcal{C}, \mathcal{H}]^T$ is the vector of dimensionless conserved variables and $\mathbf{f}(\mathbf{u}) = [f_C, f_H]^T$ is the vector of their corresponding nonlinear flux vectors. Here the flux vector functions for the dimensionless composition and enthalpy are given as

$$\mathbf{f} := f_C = f_H = \begin{cases} \mathbf{0}, & \mathcal{H} \leq 0, \\ (1 - \mathcal{C} + \mathcal{H})^m \left(\frac{\mathcal{H}}{1 - \mathcal{C} + \mathcal{H}} \right)^n \hat{\mathbf{g}}, & 0 < \mathcal{H} < \mathcal{C}. \end{cases} \tag{24}$$

Table 1. A summary of simplified thermodynamic properties as well as flow properties of water in porous ice used in present work

Parameter	Value	Units
ρ	1000	kg/m ³
$c_{p,w}$	4186	J/(kg K)
$c_{p,i}$	2106.1	J/(kg K)
κ_w	0.606	W/(m K)
κ_i	2.25	W/(m K)
L	333.55	kJ/kg
T_m	273.16	K
α_T	$1.45 \cdot 10^{-7}$	m ² /s
$\epsilon_{p,r}$	0.503	-
Ste	3.43	-
k_0	$5.56 \cdot 10^{-11}$ (Meyer and Hewitt, 2017)	m ²
k_{rw}^0	1.0	-
m	3.0	-
n	2.0	-
g	9.81	m/s ²
μ	10^{-3}	Pa s
K_h	$5 \cdot 10^{-4}$	m/s

The above analysis shows the distinct system behaviors in the different regions based on fluxes (see Figure 2). In this work, region 3 with no solid matrix is not considered since the constitutive relation for volumetric flux (Darcy's law) is not valid anymore. From Equation (24), it can be observed that the fluxes of enthalpy and composition in the system of governing equations (23) are identical in regions 1 and 2 defined by the symbol \mathbf{f} for brevity. This is the result of scaling owing to the fact that the composition changes only when water infiltrates or convects while carrying the enthalpy in form of latent heat (and specific heat) along with it.

In the next section, we will consider a simple problem of melt transport across a discontinuity to utilize the method of characteristics (MOC) for solving the system of hyperbolic partial differential equations (Lighthill and Whitham, 1955; LeVeque, 1992) given in Equation (23).

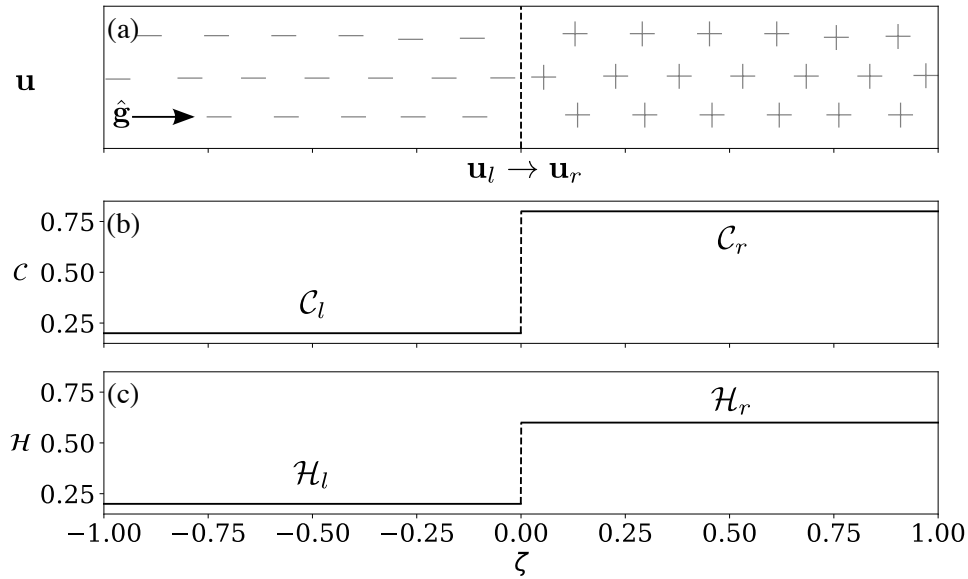


Fig. 3. One-dimensional Riemann problem: (a) Schematic representation of \mathbf{u} across a discontinuity within or at the boundary of a porous firn. Initial conditions for the Riemann problem for conserved variables (b) \mathcal{C} and (c) \mathcal{H} plotted against dimensionless depth coordinate, ζ .

3 MELT TRANSPORT ACROSS A DISCONTINUITY IN FIRN

This section considers the reaction front arising from melt flow across a discontinuity in dimensionless composition and enthalpy at a depth, say $\zeta = 0$, as shown in Figure 3. The dynamics of such problems can be understood using hyperbolic analysis of the coupled system of partial differential equations in one dimension (Lighthill and Whitham, 1955; LeVeque, 1992; Venkatraman and others, 2014; Jordan and Hesse, 2015; Ghaderi Zefreh and others, 2019).

3.1 General structure of reaction fronts

Consider the following one-dimensional initial value problem with two constant states, known as a Riemann problem. See LeVeque (1992) for a pedagogical introduction to Riemann problems and their analysis. Let the spatial dimension be the direction of gravity, $\hat{\mathbf{g}}$, which aligns with the (dimensionless) depth coordinate, z (ζ). In that case, the dimensionless flux vector (24) reduces to

$$f := \begin{cases} 0, & \mathcal{H} \leq 0 \\ (1 - \mathcal{C} + \mathcal{H})^m \left(\frac{\mathcal{H}}{1 - \mathcal{C} + \mathcal{H}} \right)^n, & 0 < \mathcal{H} < \mathcal{C} \end{cases} \quad (25)$$

The system of dimensionless composition and enthalpy conservation equations (23) can be written in one-dimensional depth coordinates, ζ , as

$$\mathbf{u}_\tau + \mathbf{f}(\mathbf{u})_\zeta = \mathbf{0}, \quad \tau \in \mathbb{R}^+, \quad \zeta \in \mathbb{R}, \quad (26)$$

with initial conditions

$$\mathbf{u} = \begin{cases} \mathbf{u}_l, & \zeta < 0 \\ \mathbf{u}_r, & \zeta > 0 \end{cases} \quad (27)$$

where the flux vector in ζ direction is $\mathbf{f}(\mathbf{u}) = [f, f]^T$ and the subscripts τ and ζ refer to the partial derivatives with respect to the dimensionless time and depth respectively. The subscripts l and r refer to the state of the system on the left and right sides of a discontinuity. During melt infiltration into firn the left (right) state corresponds to the top (bottom) layer around a discontinuity. An example of an initial discontinuity with left state, \mathbf{u}_l , and right state, \mathbf{u}_r , is shown in Figures 3*b* and 3*c*. The flow is towards the direction of gravity, assumed to be in $+\zeta$ -direction. The solution to the Riemann problem for well-behaved systems of two coupled nonlinear partial differential equations is characterized by the formation of an intermediate state, \mathbf{u}_i , bounded by two waves \mathscr{W}_1 and \mathscr{W}_2 (LeVeque, 1992). This solution structure, observed in Figure 4, can be represented as

$$\mathbf{u}_l \xrightarrow{\mathscr{W}_1} \mathbf{u}_i \xrightarrow{\mathscr{W}_2} \mathbf{u}_r \quad (28)$$

In the context of reactive meltwater transport, the waves \mathscr{W}_1 and \mathscr{W}_2 are the reaction fronts and the intermediate state, \mathbf{u}_i , corresponds to a state between the fronts. The system (26) can be recast into a

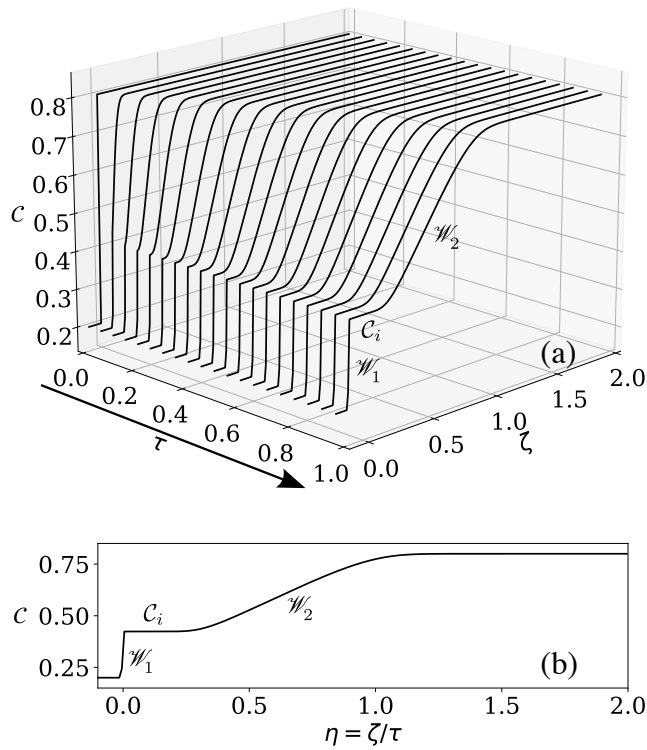


Fig. 4. Solution of the Riemann problem introduced in Figure 3. (a) Evolution of dimensionless composition, \mathcal{C} , in space, ζ , and time, τ . (b) The same self-similar solution plotted as a function of similarity variable $\eta = \zeta/\tau$.

quasilinear form using chain rule as

$$\mathbf{u}_\tau + \nabla_{\mathbf{u}} \mathbf{f}(\mathbf{u}) \mathbf{u}_\zeta = \mathbf{0} \quad (29)$$

where $\nabla_{\mathbf{u}} \mathbf{f}(\mathbf{u})$ is the gradient of flux, $\mathbf{f}(\mathbf{u})$, with respect to the conserved variables, \mathbf{u} , which takes the matrix form

$$\nabla_{\mathbf{u}} \mathbf{f}(\mathbf{u}) = \begin{bmatrix} f_{,c} & f_{,\mathcal{H}} \\ f_{,c} & f_{,\mathcal{H}} \end{bmatrix} \quad (30)$$

where the subscripts $,\mathcal{C}$ and $,\mathcal{H}$ refer to the partial derivatives with respect to dimensionless composition and enthalpy respectively. The derivatives of the flux gradient above can be evaluated explicitly, and which are given in Appendix A. The system of advection equations (29) results in waves (fronts) propagating with their characteristic velocities. These fronts have self-similar stretching patterns, because of their own characteristic velocities given by the flux gradient.

3.2 Self-similarity of reaction fronts

The recognition of the constant stretching morphology of the reaction fronts from an initial step change allows the introduction of the similarity variable

$$\eta = \frac{\zeta}{\tau} \quad (31)$$

Physically, η describes the dimensionless propagation velocity of the reaction front. The solution generally collapses into a single profile when plotted as a function of η (see Figure 4b). Therefore, the system of partial differential equations (29) can be transformed into a system of ordinary differential equations by considering the nonlinear eigenvalue problem

$$(\mathbf{A} - \lambda_p \mathbf{I}) \mathbf{r}_p = \mathbf{0}, \quad p \in \{1, 2\}, \quad (32)$$

where the flux gradient is $\mathbf{A} = \nabla_{\mathbf{u}} \mathbf{f}(\mathbf{u})$ and the eigenvector is $\mathbf{r}_p = d\mathbf{u}/d\eta$ corresponding to the eigenvalue λ_p . Here the eigenvalues λ_1 and λ_2 are the characteristic propagation speeds of the waves \mathscr{W}_1 and \mathscr{W}_2

respectively. The associated eigenvectors, $\mathbf{r}_p = d\mathbf{u}/d\eta$, give the pathways through the $\mathcal{C} - \mathcal{H}$ plane, also referred to as the hodograph plane, that satisfy the conservation equations (see Figure 5b for example).

Constant solutions of the conservation laws (29) satisfy (32) trivially because $d\mathbf{u}/d\eta = 0$. Solutions of the conservation laws (29) that vary continuously must instead satisfy the eigenvalue problem (32). Finally, discontinuities in the solution of (29) must satisfy the Rankine-Hugoniot (R-H) jump condition (LeVeque, 1992), which is derived from the discrete conservation of mass and enthalpy around the discontinuity, and given by

$$\Lambda_{\mathcal{S}}(\mathbf{u}_+, \mathbf{u}_-) = \frac{\mathbf{f}(\mathbf{u}_+) - \mathbf{f}(\mathbf{u}_-)}{\mathbf{u}_+ - \mathbf{u}_-} = \frac{[\mathbf{f}(\mathbf{u})]}{[\mathbf{u}]}, \quad (33)$$

where $\Lambda_{\mathcal{S}}$ is the shock speed, $[\cdot]$ refers to the jump condition across the shock and subscripts $+$ and $-$ refer to the state on the left and right sides of a shock wave. Note that the left (l) and right (r) states might not necessarily be the left ($-$) and right ($+$) sides of a shock front, due to the presence of an intermediate state.

3.3 Construction of the solution in the $\mathcal{C} - \mathcal{H}$ hodograph plane

The self-similar solutions are constructed by identifying directions in the $\mathcal{C} - \mathcal{H}$ hodograph plane that satisfy conservation laws and the equation of state. One such direction allows a continuous variation in \mathbf{u} , which can be found by integrating the eigenvectors of the flux gradient. Another set of directions is determined by the nonlinear algebraic system of equations arising from the R-H jump condition (33), described by shock fronts. First, we consider a system where both left state, $\mathbf{u}_l = [\mathcal{C}_l, \mathcal{H}_l]^T$, and right state, $\mathbf{u}_r = [\mathcal{C}_r, \mathcal{H}_r]^T$, reside in the same region. Then we investigate more complicated cases where left and right states can lie in different regions. Lastly we discuss the cases where a fully-saturated region forms, leading to the failure of the current hyperbolic PDE analysis. This theory is then further extended to analyze the formation and evolution of fully-saturated regions which are governed by a different, elliptic PDE (Shadab and Hesse, 2022). Although there can be at most one moving wave for simple cases where the medium remains unsaturated ($\mathcal{C} < \rho$, $\mathcal{C} < 1$ or $\phi_g > 0$), there can be two moving waves when a fully-saturated region appears, i.e., $\mathcal{C} = 1$. Below we enumerate twelve distinct self-similar solutions to the Riemann problem that describe a variety of firm hydrological processes and summarize them in Table 2.

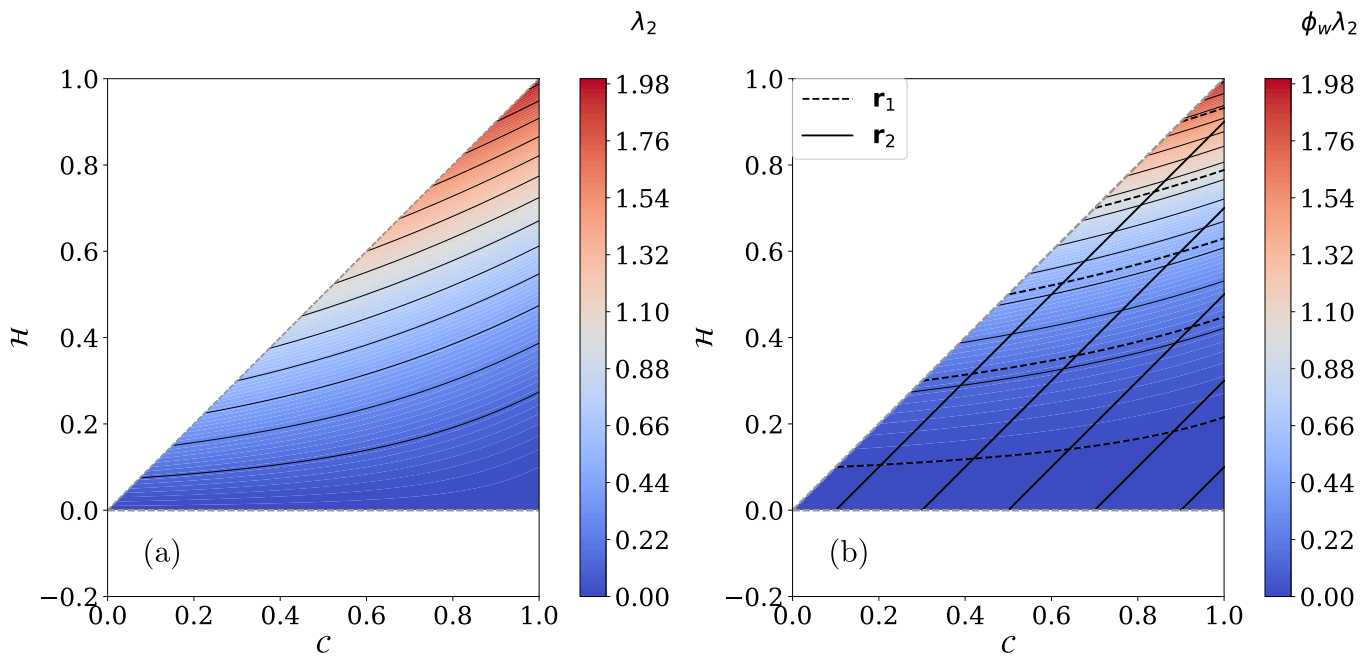


Fig. 5. Contour plots of (a) second eigenvalue, λ_2 , and (b) propagation velocity of second front with respect to the melt given by $\phi_w \lambda_2$ in the $\mathcal{C} - \mathcal{H}$ hodograph plane for $m = 3$ and $n = 2$. The slow path \mathbf{r}_1 and fast path \mathbf{r}_2 are shown with dashed and solid lines respectively in panel *b*.

3.3.1 Region 2 only (Three-phase region)

Region 2 ($0 < \mathcal{H} < \mathcal{C}$) consists of all three-phases, which is relevant for temperate glaciers where $\mathcal{T} = 0$ or $\mathcal{T} = T_m$. In the three-phase region, the eigenvalues of the flux gradient (30) are

$$\lambda_1 = 0 \quad \text{and} \quad \lambda_2 = f_{,\mathcal{C}} + f_{,\mathcal{H}} = n\mathcal{H}^{n-1}(1 - \mathcal{C} + \mathcal{H})^{m-n}. \tag{34}$$

where the subscripts \mathcal{C} and \mathcal{H} refer to the partial derivatives with respect to the corresponding conserved variable.

The first reaction front is a stationary contact discontinuity as $\lambda_1 = 0$. The eigenvalue λ_2 gives a dimensionless propagation speed of the second reaction front \mathcal{W}_2 as a function of \mathcal{C} and \mathcal{H} , as plotted in Figure 5a for $m = 3$ and $n = 2$. Therefore, all solutions governed by hyperbolic PDEs (26) will have at most a single moving reaction front. Due to variable porosity, the dimensionless system is scaled with respect to the largest saturated hydraulic conductivity, K_h , which corresponds to the volumetric flux of water (Darcy’s flux), rather than the melt velocity. Hence, the propagation speed of the second reaction

front relative to the melt is $\phi_w \lambda_2$, as shown in Figure 5*b*. As expected, the propagation velocity $\phi_w \lambda_2$ decreases towards the lower boundary of the three-phase region ($\mathcal{H} = 0$). These eigenvalues yield two corresponding, linearly independent eigenvectors in the $\mathcal{C} - \mathcal{H}$ hodograph plane given by

$$\mathbf{r}_1 = \begin{bmatrix} \frac{-f, \mathcal{H}}{f, \mathcal{C}} \\ 1 \end{bmatrix} = \begin{bmatrix} \frac{(n(1-\mathcal{C})+m\mathcal{H})}{(m-n)\mathcal{H}} \\ 1 \end{bmatrix} \quad \text{and} \quad \mathbf{r}_2 = \begin{bmatrix} \frac{f, \mathcal{H}}{f, \mathcal{H}} \\ 1 \end{bmatrix} = \begin{bmatrix} 1 \\ 1 \end{bmatrix}. \quad (35)$$

These eigenvectors can be used to find the integral curves using the system of ODEs

$$\frac{d\mathbf{u}}{d\eta} = \frac{1}{\nabla_{\mathbf{u}} \lambda_p \cdot \mathbf{r}_p} \mathbf{r}_p \quad (36)$$

which can be further integrated to obtain the solution pathways $\mathbf{u}(\mathbf{u}_0, \eta)$ as

$$\mathbf{u}(\mathbf{u}_0, \eta) = \mathbf{u}_0 + \int_{\lambda_p(\mathbf{u}_0)}^{\eta} \frac{1}{\nabla_{\mathbf{u}} \lambda_p \cdot \mathbf{r}_p} \mathbf{r}_p d\eta'. \quad (37)$$

These paths in the $\mathcal{C} - \mathcal{H}$ hodograph plane comprise the set of states that can be connected to the initial state \mathbf{u}_0 by a reaction front with a continuous variation in \mathbf{u} . In the three phase region, the family of integral curves corresponding to first eigenvector \mathbf{r}_1 is referred to as slow path as $\lambda_1 < \lambda_2$ and is given by

$$\mathcal{C} = 1 + \mathcal{H} + \mathfrak{C} \mathcal{H}^{-\frac{n}{m-n}}. \quad (38)$$

where \mathfrak{C} is the constant of integration, which can be found for the initial point \mathbf{u}_0 . The slow path lines are the same as constant flux lines, as shown in Figure 5*b*. Next, the family of integral curves corresponding to the second eigenvector is known as fast path and is given by

$$\mathcal{C} = \mathcal{H} + \mathfrak{C}. \quad (39)$$

The speed of second characteristic λ_2 is non-negative and increases monotonically in the direction of integral

curves corresponding to the second eigenvector \mathbf{r}_2 (fast paths) in three-phase region for $n > 1$ (see Lemma Appendix 1.1 and Figure 5b). Additionally, the slow path corresponds to constant flux contours as $\lambda_1 = 0$ and the fast path corresponds to constant porosity, φ , contours (Lemma Appendix 1.2).

Solutions in the three-phase region

We will now discuss the different analytical solutions within the three-phase region, tailored to glaciological scenarios. All scenarios are summarized in Table 2. The discussion below assumes that \mathbf{u}_0 is the left state, \mathbf{u}_l , and describes the set of permissible right states \mathbf{u}_r . We begin with cases that lead to solutions with a single front before considering cases leading to two fronts and the formation of an intermediate state.

(a.) Stationary linear reaction front (Case I): This case resembles a steady meltwater flux into a temperate firn with a step reduction in porosity at shallow depth (Figures 6d-f). The integral curves associated with λ_1 and \mathbf{r}_1 , known as the first characteristic field $(\lambda_1, \mathbf{r}_1)$, are constant flux lines in the $\mathcal{C} - \mathcal{H}$ hodograph plane. Any right state \mathbf{u}_r , along the integral curve, connected to \mathbf{u}_0 by a stationary discontinuity is a weak solution of Equation (29). Because $\lambda_1 = 0$, the first wave is a stationary contact discontinuity \mathcal{C}_1 . The fluxes of \mathcal{C} and \mathcal{H} on both sides are the same so that the melt transport does not change \mathcal{C} and \mathcal{H} and the front does not evolve. So, a contact discontinuity is the solution for the left and right states lying on the slow path (38) (constant flux lines) satisfying

$$\frac{\varphi_l}{\varphi_r} = \frac{1 - \mathcal{C}_l + \mathcal{H}_l}{1 - \mathcal{C}_r + \mathcal{H}_r} = \left(\frac{\mathcal{H}_l}{\mathcal{H}_r} \right)^{-\frac{n}{m-n}} \quad \text{or} \quad f(\mathbf{u}_l) = f(\mathbf{u}_r). \tag{40}$$

The complete solution in this case takes the form

$$\mathbf{u} = \begin{cases} \mathbf{u}_l, & \zeta < 0 \\ \mathbf{u}_r, & \zeta > 0 \end{cases}. \tag{41}$$

Figures 6a-c (green color) illustrate an example of a system that results in a stationary contact discontinuity. This system corresponds to a steady meltwater flux of $f = 0.112$ inside temperate porous firn with a jump in porosity from 70% at $\zeta < 0$ to 55.3% in $\zeta > 0$ (coarse-to-fine transition in firn) leading to liquid water contents of 0.4 and 0.45 respectively in these regions. These values correspond to $\mathbf{u}_l = [\mathcal{C}_l, \mathcal{H}_l]^T = [0.7, 0.4]^T$

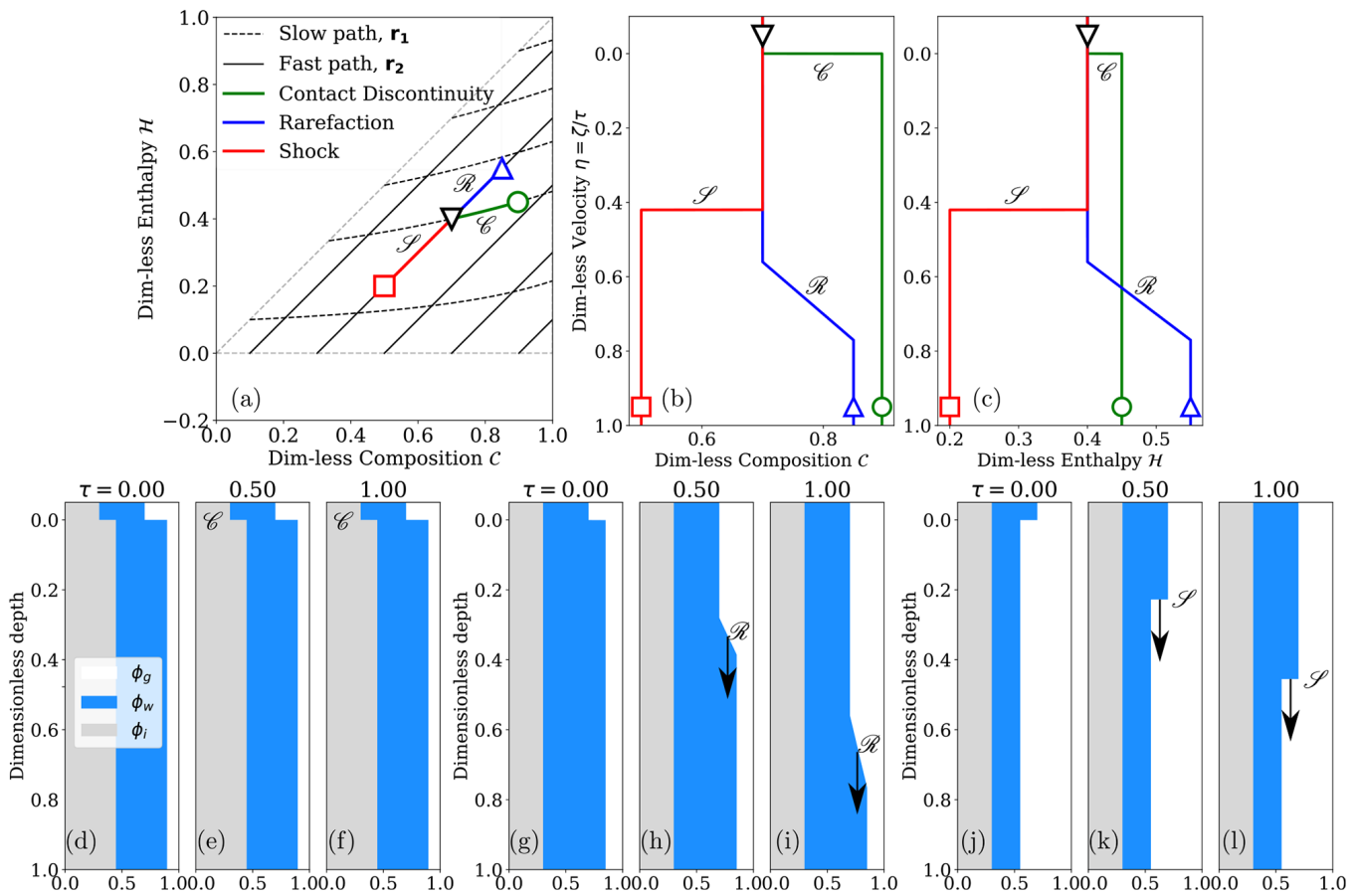


Fig. 6. The simple solutions of a Riemann problem leading to a contact discontinuity \mathcal{C} (green), rarefaction \mathcal{R} (blue), and shock waves \mathcal{S} (red). (a) Construction of solution in the hodograph plane and their corresponding self-similar analytical solutions for (b) dimensionless composition and (c) dimensionless enthalpy with dimensionless velocity η . The evolution of the volume fractions of the three phases in the system for different configurations at dimensionless times $\tau = 0, 0.5, 1.0$: (d-f) Case I - contact discontinuity, (g-i) Case II - drying front/rarefaction wave, and (j-l) Case III - wetting front/shock wave.

and right state $\mathbf{u}_r = [0.897, 0.45]^T$. The resulting system illustrated by the volume fractions of the three phases highlights a porosity jump in the temperate firm that has a constant steady meltwater flux on both sides, as shown in Figures 6d-f at different times.

(b.) Moving nonlinear reaction front: The integral curves associated with the second characteristic field (λ_2, \mathbf{r}_2) are the constant porosity φ contours. Thus, a nonlinear characteristic wave is the solution for the left and right states lying on the fast path (39) satisfying

$$C_r = C_l + (\mathcal{H}_r - \mathcal{H}_l). \tag{42}$$

(i.) Rarefaction wave (Case II): This case resembles a sudden drop of meltwater influx into a temperate firn with constant porosity (Figures 6*g-i*). If the characteristic speed λ_2 varies smoothly from left to right state, any right state \mathbf{u} along the fast path is connected to left state \mathbf{u}_0 by a continuously varying saturation front (Figure 6*a*, blue lines). The propagation velocity, λ_2 , along these continuous reaction fronts increases monotonically such that the reaction front spreads with time. These self-smoothing drying fronts are referred to as rarefaction waves, denoted by the symbol \mathcal{R} . The term drying front refers to drying due to meltwater drainage instead of refreezing (Clark and others, 2017). Rarefaction waves are a weak solution of Equation (32) if the resultant profile of \mathbf{u} is single-valued. This condition is satisfied if \mathbf{u} lies on the branch of the integral curve \mathbf{r}_2 emanating from \mathbf{u}_0 in the direction of increasing λ_2 (see Figures 5 and 6*a*, blue lines). The analytical solution concerning the self-similar variable η for a rarefaction wave on an integral curve can be evaluated from Equation (37), which comes out to be

$$\mathcal{H} = {}^{n-1}\sqrt{\frac{\eta}{n(1 - C_l + \mathcal{H}_l)^{m-n}}} \quad \text{and} \tag{43}$$

$$C = C_l - \mathcal{H}_l + {}^{n-1}\sqrt{\frac{\eta}{n(1 - C_l + \mathcal{H}_l)^{m-n}}}. \tag{44}$$

The final solution in this case takes the form

$$\mathbf{u} = \begin{cases} \mathbf{u}_l, & \eta < \lambda_2(\mathbf{u}_l) \\ \left[\begin{array}{c} C_l - \mathcal{H}_l + {}^{n-1}\sqrt{\frac{\eta}{n(1 - C_l + \mathcal{H}_l)^{m-n}}} \\ {}^{n-1}\sqrt{\frac{\eta}{n(1 - C_l + \mathcal{H}_l)^{m-n}}} \end{array} \right], & \lambda_2(\mathbf{u}_l) < \eta < \lambda_2(\mathbf{u}_r) . \\ \mathbf{u}_r, & \eta > \lambda_2(\mathbf{u}_r) \end{cases} \tag{45}$$

where the speed of the second characteristic $\lambda_2(\cdot)$ is evaluated from Equation (34). An example of this case is when meltwater flux instantly drops, leading to a smoothing drainage front. Figures 6*a-c* (blue line) show a moving rarefaction developed inside a 70% porous firn due to an instantaneous reduction in meltwater flux, captured by lower (40%) and higher (55%) liquid water content layers on top and bottom respectively.

These numbers translate to left (top) $\mathbf{u}_l = [0.7, 0.4]^T$ and right (bottom) states being $\mathbf{u}_r = [0.85, 0.55]^T$. The resulting evolution of volume fractions is shown in Figures 6*g-i*. The leading edge of the rarefaction front moves faster than the trailing edge connected by a gradual, linear smoothing. In this case, it is a linear profile (straight line) as the power law exponents in Equation (45) are $m = 3$ and $n = 2$. This drying/rarefaction front has been studied by Clark and others (2017) and was observed in models studying the Dye-2 site in Greenland on 12 August 2016 after the meltwater flux ceased (Samimi and others, 2020; Vandecrux and others, 2020; Colliander and others, 2022; Shadab and others, 2024a).

(ii.) Shock wave (Case III): This case resembles a sudden increase of meltwater influx into a temperate firn with constant porosity (Figures 6*j-l*). If the right state \mathbf{u} lies on the opposite branch of the integral curve (shown by red line in Figure 6*a* for example), a continuous reaction front would result in unphysical solutions as the characteristics will cross each other. Therefore, in this case \mathbf{u} is connected to left state \mathbf{u}_0 by a discontinuous reaction front that propagates with a velocity, $\Lambda_{\mathcal{S}}(\mathbf{u}_0, \mathbf{u})$, which can be calculated from the R-H jump condition (33) using initial conditions $(\mathbf{u}_l, \mathbf{u}_r)$. Such fronts are referred to as wetting/shock fronts, denoted by the symbol \mathcal{S} . The set of permissible right states \mathbf{u} that can be connected to the left state \mathbf{u}_0 by shocks lie on the segment of the Hugoniot-locus that satisfies the entropy condition. In the three-phase region for the system of equations considered, the Hugoniot-locus is the same as the integral curve, which is found to be the fast path \mathbf{r}_2 (39) from the Hugoniot jump condition (33), since the flux of enthalpy and composition are the same. The dimensionless velocity of the shock from Equation (33) is then

$$\Lambda_{\mathcal{S}}(\mathbf{u}_+, \mathbf{u}_-) = \frac{d\zeta}{d\tau} = \frac{f(\mathbf{u}_+) - f(\mathbf{u}_-)}{\mathcal{H}_+ - \mathcal{H}_-} = \frac{f(\mathbf{u}_+) - f(\mathbf{u}_-)}{\mathcal{C}_+ - \mathcal{C}_-}, \tag{46}$$

where the subscript $-$ refers to the left (top) state and $+$ is the right (bottom) state for this particular configuration where $f(\mathbf{u}_l) > f(\mathbf{u}_r)$. The final solution thus takes the form

$$\mathbf{u} = \begin{cases} \mathbf{u}_l, & \zeta/\tau < \Lambda_{\mathcal{S}}(\mathbf{u}_r, \mathbf{u}_l) \\ \mathbf{u}_r, & \zeta/\tau > \Lambda_{\mathcal{S}}(\mathbf{u}_r, \mathbf{u}_l) \end{cases}. \tag{47}$$

When meltwater flux instantly increases, it leads to a sharp wetting front propagating in the direction of gravity. Figures 6j-k show a moving shock front developed inside a 70% porous firn due to an instantaneous increase in meltwater flux, captured by higher (40%) and lower (20%) liquid water content ϕ_w in top and bottom layers respectively. These numbers translate to left (top) state being $\mathbf{u}_l = [0.7, 0.4]^T$ and right (bottom) state being $\mathbf{u}_r = [0.5, 0.2]^T$ sketched analytically in Figures 6a-c. The wetting front has been discussed (Colbeck, 1972; Humphrey and others, 2012; Meyer and Hewitt, 2017; Clark and others, 2017, e.g.) and observed in models (Vandecrux and others, 2020; Samimi and others, 2021; Colliander and others, 2022, e.g.) and field observations including at the Dye-2 site in Greenland on 9 August 2016 when meltwater percolates in temperate firn (Heilig and others, 2018; Samimi and others, 2020).

(c.) Two fronts with an intermediate state: The solution profile contains a single reaction front if \mathbf{u}_l and \mathbf{u}_r share the same integral curve or Hugoniot-locus. In all other cases in the three-phase region without complete saturation, a different state than left or right state forms which is referred to as an intermediate state, \mathbf{u}_i , in the hodograph plane. At this intermediate state, the solution switches from the first characteristic field $(\lambda_1, \mathbf{r}_1)$ to the second $(\lambda_2, \mathbf{r}_2)$. In other words, at the intermediate state \mathbf{u}_i , the solution changes from the stationary front along constant flux lines (slow path) to the advancing reaction front along the path of constant porosity contours (fast path) that are parallel to the upper boundary of the three-phase region ($\mathcal{H} = \mathcal{C}$). The two possible intermediate states are given by the intersections of the integral curves emanating from \mathbf{u}_l and \mathbf{u}_r (see Figure 7a for example). Only one intersection yields a physically realistic single-value solution. The correct intersection is selected by requiring that the propagation speed increases monotonically from \mathbf{u}_l and \mathbf{u}_r . A single-valued solution is ensured *if and only if* \mathbf{u}_l and \mathbf{u}_i lie on the slow path first and then \mathbf{u}_i is connected to \mathbf{u}_r along the fast path. The reactive melt transport system considered here only allows two solutions for this case:

$$\mathbf{u}_l \xrightarrow{\mathcal{C}_1} \mathbf{u}_i \xrightarrow{\mathcal{R}_2} \mathbf{u}_r \quad \text{and} \quad \mathbf{u}_l \xrightarrow{\mathcal{C}_1} \mathbf{u}_i \xrightarrow{\mathcal{S}_2} \mathbf{u}_r, \quad (48)$$

because the first characteristic is linearly degenerate and the reaction front along the slow path is always a contact discontinuity \mathcal{C}_1 . The reactive melt transport across an initial discontinuity is characterized by the formation of a reacted zone corresponding to \mathbf{u}_i that is bounded between a stationary front \mathcal{C}_1 , and an advancing front that is either a rarefaction wave \mathcal{R}_2 or a shock wave \mathcal{S}_2 . Below we will discuss these two cases.

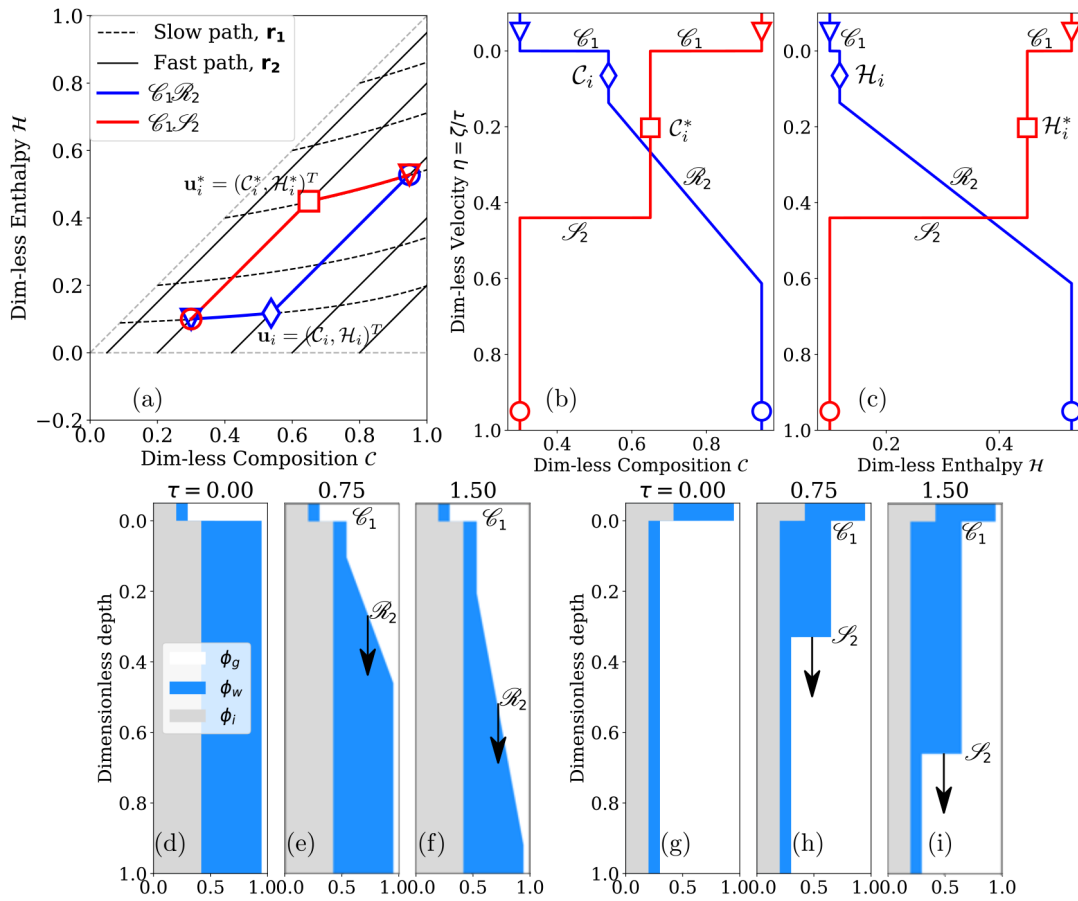


Fig. 7. Formation of an intermediate state u_i or u_i^* for Case IV - C_1R_2 or Case V - C_1S_2 respectively. An asterisk is used to differentiate the two intermediate states corresponding to the two cases. (a) Construction of solution in the hodograph plane and their corresponding self-similar analytical solutions for (b) dimensionless composition and (c) dimensionless enthalpy with dimensionless velocity η . The evolution of the volume fractions of the three phases in the system at dimensionless times $\tau = 0, 0.5, 1.0$ for the two configurations: (d-f) Case IV - C_1R_2 and (g-i) Case V - C_1S_2 .

(i.) 1-Contact discontinuity and 2-Rarefaction (Case IV): This case resembles a sudden drop in meltwater flux inside temperate firn where porosity also reduces with depth (Figure 7*d-f*). In this case $f(\mathbf{u}_l) < f(\mathbf{u}_r)$ and the resulting first characteristic wave is a contact discontinuity, \mathcal{C}_1 , which satisfies Equation (38) for left state \mathbf{u}_l and the intermediate state \mathbf{u}_i . The second characteristic wave is a rarefaction which is governed by Equations (39), (43) and (44) for intermediate state \mathbf{u}_i and right state \mathbf{u}_r . Combining all these equations results in a nonlinear algebraic equation to evaluate \mathcal{H}_i that is given by

$$1 + \mathcal{H}_r - \mathcal{C}_r - \mathcal{H}_i^{-\frac{1}{n-1}} \mathcal{H}_l^{\frac{n}{n-1}} \left(\frac{1 - \mathcal{C}_l + \mathcal{H}_l}{1 - \mathcal{C}_r + \mathcal{H}_r} \right)^{\frac{m-n}{n-1}} + \mathcal{H}_i = (1 + \mathcal{H}_l - \mathcal{C}_l) \left(\frac{\mathcal{H}_i}{\mathcal{H}_l} \right)^{-\frac{n}{m-n}} \tag{49}$$

which can be re-written in terms of porosities, φ , as

$$\varphi_r - \mathcal{H}_i^{-\frac{1}{n-1}} \mathcal{H}_l^{\frac{n}{n-1}} \left(\frac{\varphi_l}{\varphi_r} \right)^{\frac{m-n}{n-1}} + \mathcal{H}_i = \varphi_l \left(\frac{\mathcal{H}_i}{\mathcal{H}_l} \right)^{-\frac{n}{m-n}} . \tag{50}$$

Next, the composition at intermediate state, \mathcal{C}_i , can be computed from Equations (39) and (34) which corresponds to the fast path and the speed of the second characteristic, λ_2 , respectively. The final solution in this case takes the form

$$\mathbf{u} = \begin{cases} \mathbf{u}_l, & \zeta < 0 \\ \mathbf{u}_i, & 0 < \zeta/\tau < \lambda_2(\mathbf{u}_i) \\ \left[\begin{array}{c} \mathcal{C}_i - \mathcal{H}_i + n^{-1} \sqrt{\frac{\eta}{n(1-\mathcal{C}_i+\mathcal{H}_i)^{m-n}}} \\ n^{-1} \sqrt{\frac{\eta}{n(1-\mathcal{C}_i+\mathcal{H}_i)^{m-n}}} \end{array} \right], & \lambda_2(\mathbf{u}_i) < \eta < \lambda_2(\mathbf{u}_r) \\ \mathbf{u}_r, & \eta > \lambda_2(\mathbf{u}_r) \end{cases} . \tag{51}$$

Physically, the first contact discontinuity represents the constant flux of water entering the bottom, low porosity layer (Figures 7*e,f*). The rarefaction shows the drainage of the wetter firn due to gravity. Figure 7*a* shows the construction of the solution $\mathcal{C}_1\mathcal{R}_2$ in the blue line for the left (top) state which is more porous $\varphi_l = 80\%$, and has less water content (LWC) $\phi_{w,l} = 0.1$. The right (bottom) state is less porous $\varphi_r = 58\%$ but has more liquid water content $\phi_{w,r} = 0.528$. These values correspond to left and right states being

$\mathbf{u}_l = (0.3, 0.1)^T$ and $\mathbf{u}_r = (0.948, 0.528)^T$ respectively shown in Figures 7a-c. The intermediate state comes out to be $\mathbf{u}_i = (0.538, 0.117)^T$ which corresponds to LWC $\phi_{w,i} = 11.7\%$ and the same porosity as the right state, i.e., $\varphi_i = 58.0\%$. Figures 7b and 7c show the corresponding self-similar analytical solutions for composition and enthalpy respectively for this case with blue lines which only depend on the dimensionless velocity. The rarefaction moves down with a characteristic velocity that can be computed analytically. Figures 7d-f show the resulting evolution of volume fraction of each phase at different times showing self-similar expansion of the rarefaction wave.

(ii.) 1-Contact discontinuity and 2-Shock (Case V): This case is similar to Case IV but with a sudden rise in meltwater flux (Figure 7g-i), and as such $f(\mathbf{u}_l) > f(\mathbf{u}_r)$. As a result, the first characteristic wave is a contact discontinuity, \mathcal{C}_1 , that satisfies Equation (38) for the left state \mathbf{u}_l and intermediate state \mathbf{u}_i . Since the second characteristic lies on the Hugoniot locus, the result is a shockwave, \mathcal{S}_2 , which satisfies the Hugoniot-jump condition (33) for the intermediate state and right state. Combining Equations (38) and (39) gives a simple relation for dimensionless enthalpy at intermediate state, \mathcal{H}_i , to be

$$\mathcal{H}_i = \mathcal{H}_l \left(\frac{\varphi_l}{\varphi_r} \right)^{\frac{m-n}{n}} = \mathcal{H}_l \left(\frac{1 + \mathcal{H}_l - \mathcal{C}_l}{1 + \mathcal{H}_r - \mathcal{C}_r} \right)^{\frac{m-n}{n}}. \tag{52}$$

Then Equation (39) for the intermediate state, \mathbf{u}_i , and right state, \mathbf{u}_r , provides the value of dimensionless composition at intermediate state, \mathcal{C}_i . The final solution in this case takes the form

$$\mathbf{u} = \begin{cases} \mathbf{u}_l, & \zeta < 0 \\ \mathbf{u}_i, & 0 < \zeta/\tau < \Lambda_{\mathcal{S}_2}(\mathbf{u}_i, \mathbf{u}_r) \\ \mathbf{u}_r, & \zeta/\tau > \Lambda_{\mathcal{S}_2}(\mathbf{u}_i, \mathbf{u}_r) \end{cases} \tag{53}$$

Physically, the first contact discontinuity represents the increased, constant flux of water entering the bottom, low porosity layer. The second shock shows the wetting front advancing the water content to dryer firm because of gravity (Figures 7h,i). Figure 7a shows the construction of the solution $\mathcal{C}_1\mathcal{S}_2$ with red line for the left state which is less porous, i.e., $\varphi_l = 58.0\%$, but has more water content ($\phi_{w,l} = 52.8\%$), and the right state is more porous and less wet corresponding to $\varphi_r = 80\%$ and LWC $\phi_{w,r} = 10\%$.

These values correspond to $\mathbf{u}_l = (0.948, 0.528)^T$ and $\mathbf{u}_r = (0.3, 0.1)^T$ in Figures 7*a-c*. The intermediate state comes out to be $\mathbf{u}_i^* = (0.648, 0.448)^T$ which corresponds to the wetter intermediate region behind the wetting front with LWC $\phi_{w,i} = 44.8\%$ but the same porosity as the right state, i.e., $\varphi_i = 80\%$ (see Figures 7*g-i*). Figures 7*b* and 7*c* show the corresponding self-similar analytical solutions for composition and enthalpy respectively for this case with red lines which only depend on the dimensionless velocity.

(d.) Two fronts and a jump with two intermediate states (formation of a saturated region, Case VI): This case resembles a temperate firm with a step decrease in porosity at depth receiving a sudden increase of meltwater influx (Figure 8*d-f*), which results in ponding at the porosity contrast and a rising water table. The initial conditions of this case are similar to Case V ($\mathcal{C}_1\mathcal{S}_2$). However, in this case, the slow path emanating from the left state does not intersect with the fast path from the right state in the three-phase region where $\mathcal{C} < 1$, as shown in Figure 8*a*. In other words, the bottom layer is unable to accommodate the flux of meltwater from the top layer, as discussed for soils in Shadab and Hesse (2022). If the intermediate state leads to complete saturation, i.e., $\mathcal{C}_i = 1$, then the proposed hyperbolic PDE solution framework breaks down. This happens because inside the fully-saturated region, the dynamics of the water phase change from gravity-driven to pressure-driven as the governing model changes from hyperbolic (local) to elliptic (global) partial differential equations (see Shadab and Hesse (2022) for a detailed analysis). In this case, the dynamics becomes complicated as the complete solution cannot be directly interpreted from the hodograph plane because the flux in the saturated region may not simply be the hydraulic conductivity (24) anymore.

Nevertheless, we can still construct a full analytical solution to this problem using the extended kinematic wave approximation proposed by Shadab and Hesse (2022). In this case, the solution consists of three waves including a backfilling shock moving upwards (Figures 8*d-f*), denoted by symbol \mathcal{S}_1^* , a stationary jump at the initial location of the jump, denoted by \mathcal{J}_2 , and a downward moving shock (wetting front), \mathcal{S}_3 , into the less porous and temperate layer. Note that the jump \mathcal{J}_2 lies in the saturated region and therefore does not represent any hyperbolic wave. Therefore, it is represented by a broken arrow in the full solution given by

$$\mathbf{u}_l \xrightarrow{\mathcal{S}_1^*} \mathbf{u}_{i1} \overset{\mathcal{J}_2}{\dashrightarrow} \mathbf{u}_{i2} \xrightarrow{\mathcal{S}_3} \mathbf{u}_r.$$

The solution is explained in detail as follows and illustrated in Figures 8*a-c*. First, the backfilling shock on the fast path (constant porosity line) connects to the first intermediate state, i_1 , which lies on the line $\mathcal{C} = 1$. Therefore, the first intermediate state variables are

$$\mathcal{C}_{i_1} = 1 \quad \text{and} \quad \mathcal{H}_{i_1} = 1 - \mathcal{C}_l + \mathcal{H}_l. \quad (54)$$

This state is observed right next to the left state and can be considered as the rising perched water table in the region $\zeta < 0$. The speed of this backfilling, upper shock in dimensionless form is again given by the Rankine-Hugoniot jump condition as

$$\Lambda_{\mathcal{J}_1^*} = \frac{d\zeta_U}{d\tau} = \frac{f(\mathbf{u}_l) - q_s(\tau)}{\mathcal{H}_l - \mathcal{H}_{i_1}} = \frac{f(\mathbf{u}_l) - q_s(\tau)}{\mathcal{C}_l - \mathcal{C}_{i_1}} < 0, \quad (55)$$

where ζ_U is the location of the upper shock. The shock moves upwards due to choking as the numerator is positive, because flux $f(\mathbf{u}_l)$ is larger than the time-dependent dimensionless flux in the saturated region, $q_s(\tau)$, which is also scaled by K_h . Note that the flux in the saturated region $q_s(\tau)$ is not the saturated hydraulic conductivity but instead, it is governed by the dynamics of the saturated region.

Next, the first intermediate state i_1 is connected to the second intermediate state i_2 through a stationary jump \mathcal{J}_2 at the location of initial jump at $\zeta = 0$. Both intermediate states lie in the fully-saturated region and therefore the jump \mathcal{J}_2 does not represent a hyperbolic wave. The flux inside the isothermal saturated region $q_s(\tau)$ is found to be uniform in this case (Shadab and Hesse, 2022). Therefore, the flux between the two intermediate states is also same, equal to $q_s(\tau)$. The state variables \mathcal{C} and \mathcal{H} for the second intermediate state, i_2 , are provided by the right state. The second intermediate state also lies at $\mathcal{C} = 1$ on the fast path (39) (Hugoniot locus) emanating from right state, i.e., $\mathcal{C}_r - \mathcal{H}_r = \mathcal{C}_{i_2} - \mathcal{H}_{i_2}$. Therefore, the second intermediate state variables are simply,

$$\mathcal{C}_{i_2} = 1 \quad \text{and} \quad \mathcal{H}_{i_2} = 1 - \mathcal{C}_r + \mathcal{H}_r. \quad (56)$$

Similarly, the velocity of the downward-moving lower shock (wetting front) is

$$\Lambda_{\mathcal{S}_3} = \frac{d\zeta_L}{d\tau} = \frac{q_s(\tau) - f(\mathbf{u}_r)}{\mathcal{C}_{i_2} - \mathcal{C}_r} = \frac{q_s(\tau) - f(\mathbf{u}_r)}{1 - \mathcal{C}_r} > 0 \tag{57}$$

where ζ_L is the dimensionless location of the lower shock. Similar to a two-layer soil discussed in Shadab and Hesse (2022), the dimensionless flux in the saturated region is a depth-based harmonic mean of the dimensionless saturated hydraulic conductivities at the two intermediate states given by

$$q_s(\tau) = \frac{\zeta_U(\tau) - \zeta_L(\tau)}{\frac{\zeta_U(\tau)}{K_{i_1}} - \frac{\zeta_L(\tau)}{K_{i_2}}}, \tag{58}$$

where K_{i_1} and K_{i_2} are the dimensionless saturated hydraulic conductivities at the first and second intermediate states given by

$$K_{i_1} = \varphi_{i_1}^m = (1 - \mathcal{C}_l + \mathcal{H}_l)^m \quad \text{and} \quad K_{i_2} = \varphi_{i_2}^m = (1 - \mathcal{C}_r + \mathcal{H}_r)^m \tag{59}$$

using Equations (54) and (56). Note that the porosities at the first and second intermediate states are the porosities of the left and right state respectively. Solving the system of coupled ordinary differential equations (57) & (55) along with the definition of flux in the saturated region (58) gives the location of the shocks and the flux in the saturated region. Similar to the case of two-layered soils in Shadab and Hesse (2022), to find the analytic value of $q_s(\tau)$, the ratio of shock speeds can be considered a constant as an ansatz given by

$$\frac{\Lambda_{\mathcal{S}_1^*}}{\Lambda_{\mathcal{S}_3}} = \frac{\zeta_U(\tau)}{\zeta_L(\tau)} = \mathfrak{R} \quad \text{for} \quad 0 < \tau \leq \tau_p. \tag{60}$$

where \mathfrak{R} is the constant ratio of shock speeds which is negative and τ_p is the dimensionless time of ponding when the upward moving shock reaches to the surface. In the special case when this jump condition happens to exist at the surface, $\mathfrak{R} = 0$, $\tau_p = 0$ and $q_s = K_{i_2}$ which is saturated hydraulic conductivity of the second intermediate state. Otherwise, by substituting equations from the shock speed ratio definition (60), shock speeds (55) and (57), and flux in the saturated region (58), \mathfrak{R} comes out to be the solution of a quadratic equation

$$\mathfrak{R}(\mathbf{u}_l, \mathbf{u}_r) = \frac{-b - \sqrt{b^2 - 4ac}}{2a} \quad \text{where} \tag{61}$$

$$a = \left(\frac{1 - \mathcal{C}_l}{1 - \mathcal{C}_r}\right) \left[1 - \left(\frac{1 - \mathcal{C}_r + \mathcal{H}_r}{1 - \mathcal{C}_l + \mathcal{H}_l}\right)^m \left(\frac{\mathcal{H}_r}{1 - \mathcal{C}_r + \mathcal{H}_r}\right)^n\right],$$

$$b = -\left(\frac{1 - \mathcal{C}_l}{1 - \mathcal{C}_r}\right) \left[1 - \left(\frac{\mathcal{H}_r}{1 - \mathcal{C}_r + \mathcal{H}_r}\right)^n\right] + \left(\frac{\mathcal{H}_l}{1 - \mathcal{C}_l + \mathcal{H}_l}\right)^n - 1 \quad \text{and}$$

$$c = 1 - \left(\frac{1 - \mathcal{C}_l + \mathcal{H}_l}{1 - \mathcal{C}_r + \mathcal{H}_r}\right)^m \left(\frac{\mathcal{H}_l}{1 - \mathcal{C}_l + \mathcal{H}_l}\right)^n.$$

Subsequently, substituting Equations (59) and (60) in (58) gives the time-invariant dimensionless flux in the saturated region q_s during $0 < \tau \leq \tau_p$ as

$$q_s = \frac{\mathfrak{R} - 1}{\mathfrak{R}/(1 - \mathcal{C}_l + \mathcal{H}_l)^m - 1/(1 - \mathcal{C}_r + \mathcal{H}_r)^m}. \tag{62}$$

The time and space invariant flux q_s leads to the result using Equations (55) and (57) that the shock speeds are constant for $0 < \tau \leq \tau_p$. Therefore, the shock locations before ponding vary linearly with time. Lastly, the full solution for this case can be summarized as

$$\mathbf{u} = \begin{cases} \mathbf{u}_l, & \zeta < \Lambda_{\mathcal{S}_1^*} \\ \mathbf{u}_{i_1} = \begin{bmatrix} 1 \\ 1 - \mathcal{C}_l + \mathcal{H}_l \end{bmatrix}, & \Lambda_{\mathcal{S}_1^*} < \zeta/\tau < 0 \\ \mathbf{u}_{i_2} = \begin{bmatrix} 1 \\ 1 - \mathcal{C}_r + \mathcal{H}_r \end{bmatrix}, & 0 < \zeta/\tau < \Lambda_{\mathcal{S}_3} \\ \mathbf{u}_r, & \zeta/\tau > \Lambda_{\mathcal{S}_3} \end{cases}. \tag{63}$$

Here the shock speeds $\Lambda_{\mathcal{S}_1^*}$ and $\Lambda_{\mathcal{S}_3}$ depend on both left and right states due to formation of the saturated region as the flux is governed by an elliptic PDE. In terms of firm processes, the lower (low porosity) layer is unable to accommodate the flux of water from the upper layer and therefore leads to a rising perched water table as well as a wetting front (Figures 8e,f). In this example, the top layer has 50% porosity and 40% liquid water content ($\phi_{w,l}$) and the bottom layer is 30% porous and has only 10% LWC. These values

correspond to left and right states being $\mathbf{u}_l = (0.9, 0.4)^T$ and $\mathbf{u}_r = (0.8, 0.1)^T$ respectively (Figures 8a-c). Consequently, the first and second intermediate states, $\mathbf{u}_{i_1} = (1, 0.5)^T$ and $\mathbf{u}_{i_2} = (1, 0.3)^T$ respectively, lie in the expanding saturated region (Figures 8d-f). The speeds of both fronts \mathcal{S}_1^* and \mathcal{S}_3 are constant before ponding occurs.

3.3.2 Region 1 only (Ice and gas region), Case VII

While the previous cases consisted of temperate firn, this case resembles a cold firn with a step reduction in porosity at depth (e.g. porous firn on top of less porous firn or glacier ice), and no meltwater influx, resulting in a dry, static system Figures 9d-f. In region 1 ($\mathcal{H} \leq 0$), since both fluxes are zero the system is not strictly hyperbolic and leads to a single wave. As the characteristic speed, λ_p , is constant, this wave is linearly degenerate and since $\lambda_1 = \lambda_2 = 0$, the characteristic is stationary. The resulting wave is a stationary contact discontinuity \mathcal{C} . There won't be any transport between the two states since the fluxes of both composition and enthalpy are zero on either side. In other words, \mathbf{u}_l will be connected to \mathbf{u}_r by a stationary contact discontinuity \mathcal{C} as

$$\mathbf{u}_l \xrightarrow{\mathcal{C}} \mathbf{u}_r.$$

The resulting solution thus takes the form

$$\mathbf{u} = \begin{cases} \mathbf{u}_l, & \zeta < 0 \\ \mathbf{u}_r, & \zeta > 0 \end{cases}. \tag{64}$$

In this example, a temperate, 40% porous firn lies on top of a cold ($T = -19.8^\circ\text{C}$), 20% porous firn corresponding to $\mathbf{u}_l = (0.6, 0.0)^T$ and $\mathbf{u}_r = (0.8, -0.1)^T$, as shown in Figures 9a-c (blue lines) and 9d-f. However, in reality the firn may compact due to overburden (Cuffey and Paterson, 2010) which is not considered in the present model. Note that the temperatures (not shown) in the two layers are the same as the initial condition with sharp transition at $\zeta = 0$ due to the absence of heat conduction.

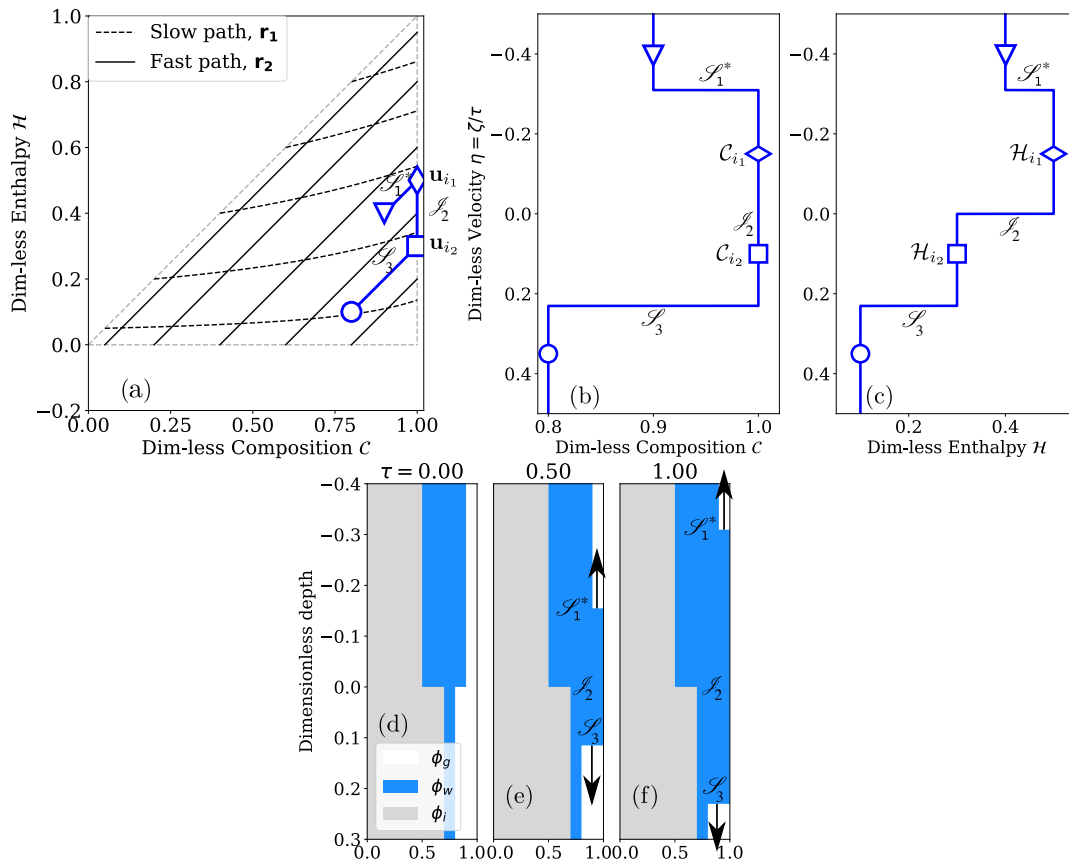


Fig. 8. Formation of a fully-saturated region in temperate firm (Case VI): (a) Construction of solution in the hodograph plane and their corresponding self-similar analytical solutions for (b) dimensionless composition and (c) dimensionless enthalpy with dimensionless velocity η . The result shown with dark blue line consists of a backfilling shock, \mathcal{S}_1^* , a jump, \mathcal{S}_2 , and another wetting shock, \mathcal{S}_3 , along with two intermediate states $\mathbf{u}_{i_1} = (\mathcal{C}_{i_1}, \mathcal{H}_{i_1})^T$ and $\mathbf{u}_{i_2} = (\mathcal{C}_{i_2}, \mathcal{H}_{i_2})^T$. The left and right states are $\mathbf{u}_l = (0.9, 0.4)^T$ and $\mathbf{u}_r = (0.8, 0.1)^T$ respectively. The first and second intermediate states, $\mathbf{u}_{i_1} = (1, 0.5)^T$ and $\mathbf{u}_{i_2} = (1, 0.3)^T$ respectively. The evolution of the volume fractions of the three phases in the resulting system at dimensionless times (d) $\tau = 0$, (e) 0.5, (f) 1.0.

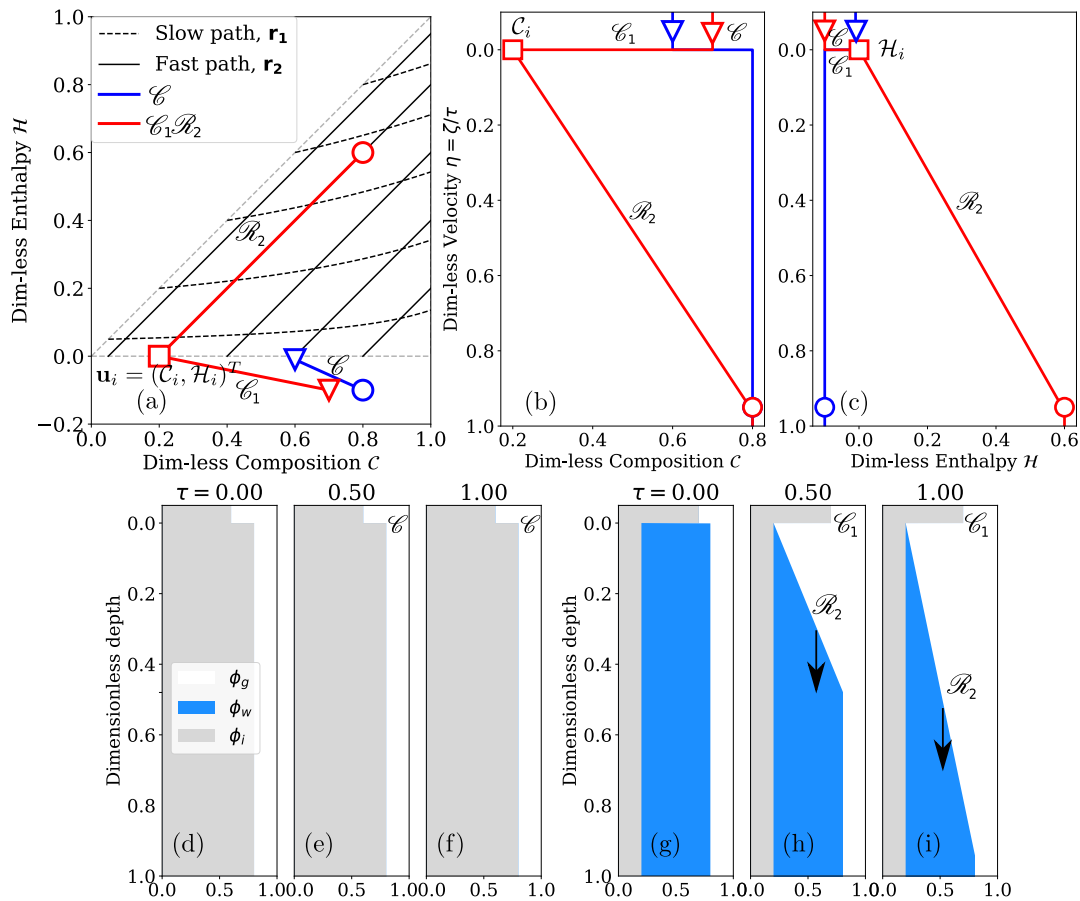


Fig. 9. Solutions when the left state lies in Region 1 (ice and gas): either only a contact discontinuity appears (Case VII) or an intermediate state, \mathbf{u}_i , along with a rarefaction wave \mathcal{R}_2 also forms in a $\mathcal{C}_1\mathcal{R}_2$ fashion (Case VIII). (a) Construction of solution in the hodograph plane and their corresponding self-similar analytical solutions for (b) dimensionless composition and (c) dimensionless enthalpy with dimensionless velocity η . Blue and red lines respectively show the solutions when the right states are in Regions 1 and 2 respectively. The evolution of the volume fractions of the three phases in the resulting system at dimensionless times $\tau = 0, 0.5, 1.0$ for the two configurations: (d-f) Case VII - \mathcal{C} and (g-i) Case VIII - $\mathcal{C}_1\mathcal{R}_2$.

3.4 Solutions transitioning between regions

3.4.1 From Region 1 (ice and gas) to Region 2 (three-phase region), Case VIII

This case resembles a dry, porous cold firn layer on top of wet temperate firn (Figure 9*g-f*), without additional meltwater influx. In this case, the left state lies in region 1 corresponding to the cold firn and the right state resides in the three-phase region (region 2). The result is a contact discontinuity \mathcal{C}_1 onto the lower boundary of the three-phase region ($\mathcal{H} = 0$) where the intermediate state lies (see Figure 9*a* for example), i.e.,

$$\mathcal{H}_i = 0. \quad (65)$$

Moreover, the intermediate state, \mathcal{C}_i , lies on the fast path (constant porosity line) in region 2 satisfying Equation (39) which gives

$$\mathcal{C}_i = \mathcal{C}_r - \mathcal{H}_r. \quad (66)$$

Simultaneously, the intermediate state is connected to the right state on the fast path, resulting in a rarefaction wave \mathcal{R}_2 . It is important to note that the second wave, \mathcal{W}_2 , is supposed to be faster than the first and that is why the slow path is avoided in the three-phase region (region 2). The final solution to this case is the same as given in Equation (51).

As an example, the left state corresponds to a 30% porous cold layer at $T = -22.63^\circ\text{C}$ lying on top of the layer corresponding to wet, temperate firn similar to liquid storage with 80% porosity and 60% LWC ($\phi_{w,r}$), as shown in Figure 9*g*. This configuration corresponds to $\mathbf{u}_l = (0.7, -0.1)^T$ and $\mathbf{u}_r = (0.8, 0.6)^T$ with intermediate state $\mathbf{u}_i = (0.2, 0.0)^T$ (Figure 9*a*, red line). As a result, the porosity jump remains stationary but the liquid storage drains downwards due to gravity forming a self-similar rarefaction wave as shown in Figures 9*b-c* (red lines) and 9*g-i*. In a nutshell, this case describes the evolution of a more saturated firn layer below a previously formed less permeable, cold frozen fringe.

3.4.2 From Region 2 (three-phase region) to Region 1 (ice and gas)

This corresponds to temperate and wet firn overlying initially cold firn (see Figures 10-12). In this case, the left state corresponding to the top layer lies in the three-phase region (region 2) and the right state corresponding to the bottom layer lies in region 1. Note that the temperature remains subzero only in the cold region (region 1, $\mathcal{H} < 0$) which lies only in the right state with a sharp transition from the left or intermediate state as heat conduction is not considered in this model. There can be four scenarios corresponding to this initial condition:

(i.) Shock (Case IX): This case corresponds to a sudden increase in meltwater flux into temperate, wet firn overlying cold firn, resulting in meltwater percolation into the deeper layers and formation of a frozen fringe (Figures 10*d-f*). When the right state in region 1 lies on the fast path in region 2 (three-phase region) extended to region 1 (ice and gas region) referred to as *extended fast path*, it results in only a single moving shock \mathcal{S} (see Figure 10*a*, blue line). Note that the extended fast paths are not the constant porosity contours in Region 1 (Figures 1*c,g*). Mathematically, the left and right states are connected by the relation

$$\mathcal{C}_r = \mathcal{H}_r + \mathcal{C}_l - \mathcal{H}_l. \quad (67)$$

The shock speed $\Lambda_{\mathcal{S}}$ can then be evaluated using the Rankine-Hugoniot condition (46). The final solution of this case is provided in Equation (47). Physically, the water seeps from the top layer to the bottom layer due to gravity and a part of it precipitates due to heat loss to the surrounding cold firn. Since the flux in the right state is zero, the evaluation depends on the difference of either dimensionless composition or enthalpy. Figures 10*a-c* (blue line) shows an example of the solution where temperate firn with 45% porosity (φ_l) and 25% LWC ($\phi_{w,l}$) initially lies on a cold layer of porosity 50% at $T = -15.84^\circ\text{C}$ (Figure 10*d*). These initial conditions correspond to a left state, $\mathbf{u}_l = (0.8, 0.25)^T$ and a right state $\mathbf{u}_r = (0.5, -0.05)^T$ (Figures 10*a-c*, blue line). A refreezing shock \mathcal{S} that results moves downwards while warming up the surrounding snow by partially refreezing (Figures 10*d-f*). This reduces the porosity behind the wetting front from 50% to 45%, equal to the same value as the left state thereby extending the previously formed frozen fringe in the top layer into the bottom layer.

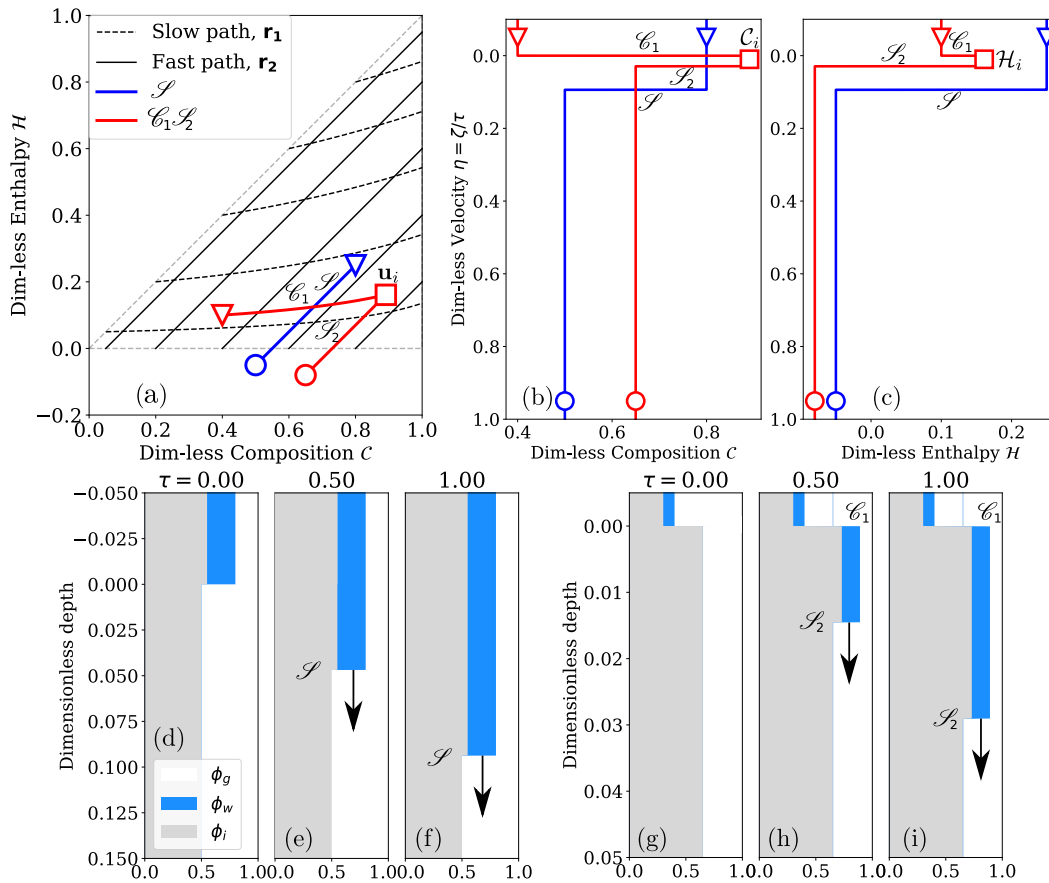


Fig. 10. Solutions when the left state lies in region 2 (three-phase) and the right state lies in region 1 without formation of saturated regions: either only a refreezing front \mathcal{S} (Case IX) appears or a contact discontinuity, \mathcal{C}_1 , an intermediate state, \mathbf{u}_i , along with a refreezing front \mathcal{S}_2 forms in a $\mathcal{C}_1\mathcal{S}_2$ (Case X) fashion. (a) Construction of solution in the hodograph plane and their corresponding self-similar analytical solutions for (b) dimensionless composition and (c) dimensionless enthalpy with dimensionless velocity η . Red and blue lines respectively show the solutions when the right states are in region 2 and region 1 respectively. The evolution of the volume fractions of the three phases in the resulting system at dimensionless times $\tau = 0, 0.5, 1.0$ for the two configurations: (d-f) Case VII - \mathcal{C} and (g-i) Case VIII - $\mathcal{C}_1\mathcal{R}_2$.

(ii.) **1-Contact discontinuity and 2-Shock (Case X):** This is similar to Case IX (wet firn overlying cold firn), but with a decreased porosity in the underlying cold firn leading to formation of a frozen fringe (Figures 10*g-i*). Here, the left state cannot be directly connected to the right state along the extended fast path as discussed in Case IX. So in this case, the left state \mathbf{u}_l in region 2 is more porous and connected to an intermediate state, \mathbf{u}_i , along the slow path where the dimensionless composition of the intermediate state, \mathcal{C}_i , is less than unity, to keep the medium unsaturated (see Figure 10*a*, red line). Similar to the only shock \mathcal{S} case (Case IX), the intermediate state lies on the extended fast path from region 2 to region 1. Therefore the solution is a combination of a stationary contact discontinuity \mathcal{C}_1 and a moving shock \mathcal{S}_2 . The first characteristic wave, contact discontinuity \mathcal{C}_1 , satisfies Equation (38) for left state \mathbf{u}_l and intermediate state \mathbf{u}_i . Since the second characteristic lies on the Hugoniot locus, a shockwave \mathcal{S}_2 results, that satisfies the Hugoniot-jump condition (33) for the intermediate state \mathbf{u}_i and right state \mathbf{u}_r . Combining all these equations gives a simple relation for dimensionless enthalpy and composition at the intermediate state as

$$\mathcal{H}_i = \mathcal{H}_l \left(\frac{1 - \mathcal{C}_l + \mathcal{H}_l}{1 - \mathcal{C}_r + \mathcal{H}_r} \right)^{\frac{m-n}{n}} \quad \text{and} \quad \mathcal{C}_i = \mathcal{H}_i + \mathcal{C}_r - \mathcal{H}_r. \tag{68}$$

The dimensionless velocity of the shock wave \mathcal{S}_2 (refreezing front) is

$$\Lambda_{\mathcal{S}_2} = \frac{f(\mathbf{u}_i) - f(\mathbf{u}_r)}{\mathcal{H}_i - \mathcal{H}_r} = \frac{\mathcal{H}_i^n (1 - \mathcal{C}_i + \mathcal{H}_i)^{m-n}}{\mathcal{H}_i - \mathcal{H}_r} \quad (\text{since } f(\mathbf{u}_r) = 0). \tag{69}$$

The full solution is given in Equation (53) with shock speed (69). Since $\mathcal{H}_r < 0$, $\mathcal{H}_i > 0$ and $f(\mathbf{u}_r) = 0$, the speed of the refreezing front \mathcal{S}_2 is slower than the temperate firn case (Case V) due to refreezing. Figures 10*a-c* (red line) shows an example of such a solution for light rainfall on a multilayered firn with coarse to fine transition. The left state corresponds to the wetter, temperate firn on top with a porosity of 70% and a liquid water content $\phi_{w,l} = 0.1$. The right state corresponds to a cold and dry firn layer with 35% porosity and a temperature of $T = -19.49^\circ\text{C}$. These values for left and right states correspond to states being $\mathbf{u}_l = (0.4, 0.1)^T$ and $\mathbf{u}_r = (0.65, -0.08)^T$, respectively. Here, a stationary contact discontinuity \mathcal{C}_1 stays at the surface leading to a growing intermediate state $\mathbf{u}_i = (0.893, 0.163)$ formed due to partial refreezing of the rainwater which warms the surrounding firn (Figures 10*g-i*). The intermediate state with

27% porosity and 16.3% LWC expands with time as the refreezing front \mathcal{S}_2 infiltrates further into the right state. Note that the porosity in the intermediate state is smaller than the right state which decreases further due to meltwater refreezing leading to the formation of a fresh frozen fringe. This phenomenon has been observed in the model by Meyer and Hewitt (2017) who used the dimensional form of Equation (69) with distinct densities of ice and water phases to explain the field data from Humphrey and others (2012).

(iii.) 1-Backfilling shock, 2-Jump and 3-Shock (formation of a saturated region, Case XI):

This is similar to Case X, where wet and temperate firn layer lies on top of cold and less porous firn, and the system receives sudden increase in meltwater flux (Figures 11 *d-f*). However, the temperature of the underlying cold firn is reduced, and the liquid water content in the above temperate layer increased which leads to the formation of a rising perched water table. The slow path originating from the left state and the extended fast path emanating from the right state do not intersect where $\mathcal{C} < 1$, making it different from Case X. If the intermediate state lies on the saturated region, then the hyperbolic nature of the solution breaks down, similar to Case VI for temperate firn (see Table 2). So the analytic solution (63) is the same as provided for the temperate firn (Case VI) consisting of a backfilling shock \mathcal{S}_1^* moving upwards with speed (55), a stationary jump \mathcal{S}_2 at the location of initial jump $\zeta = 0$ and a “refreezing” front \mathcal{S}_3 moving downwards with speed provided in Equation (57). The flux in the saturated region q_s is again provided by Equation (58). Note that the flux at the right state is $f(\mathbf{u}_r) = 0$ since it lies in region 1. Invoking the ansatz for a constant shock speed ratio, similar to Case VI, provides an analytic relation for a constant flux in the saturated region, q_s , same as Equation (62) with both shocks moving in opposite directions at constant speeds. However since the flux at the right state is zero, the relation for the ratio of shock speeds, \mathfrak{R} , earlier provided by Equation (61), now simplifies to

$$\begin{aligned} \mathfrak{R}(\mathbf{u}_l, \mathbf{u}_r) &= \frac{-b - \sqrt{b^2 - 4ac}}{2a} \quad \text{where} & (70) \\ a &= \left(\frac{1 - \mathcal{C}_l}{1 - \mathcal{C}_r} \right), \\ b &= - \left(\frac{1 - \mathcal{C}_l}{1 - \mathcal{C}_r} \right) + \left(\frac{\mathcal{H}_l}{1 - \mathcal{C}_l + \mathcal{H}_l} \right)^n - 1 \quad \text{and} \\ c &= 1 - \left(\frac{1 - \mathcal{C}_l + \mathcal{H}_l}{1 - \mathcal{C}_r + \mathcal{H}_r} \right)^m \left(\frac{\mathcal{H}_l}{1 - \mathcal{C}_l + \mathcal{H}_l} \right)^n. \end{aligned}$$

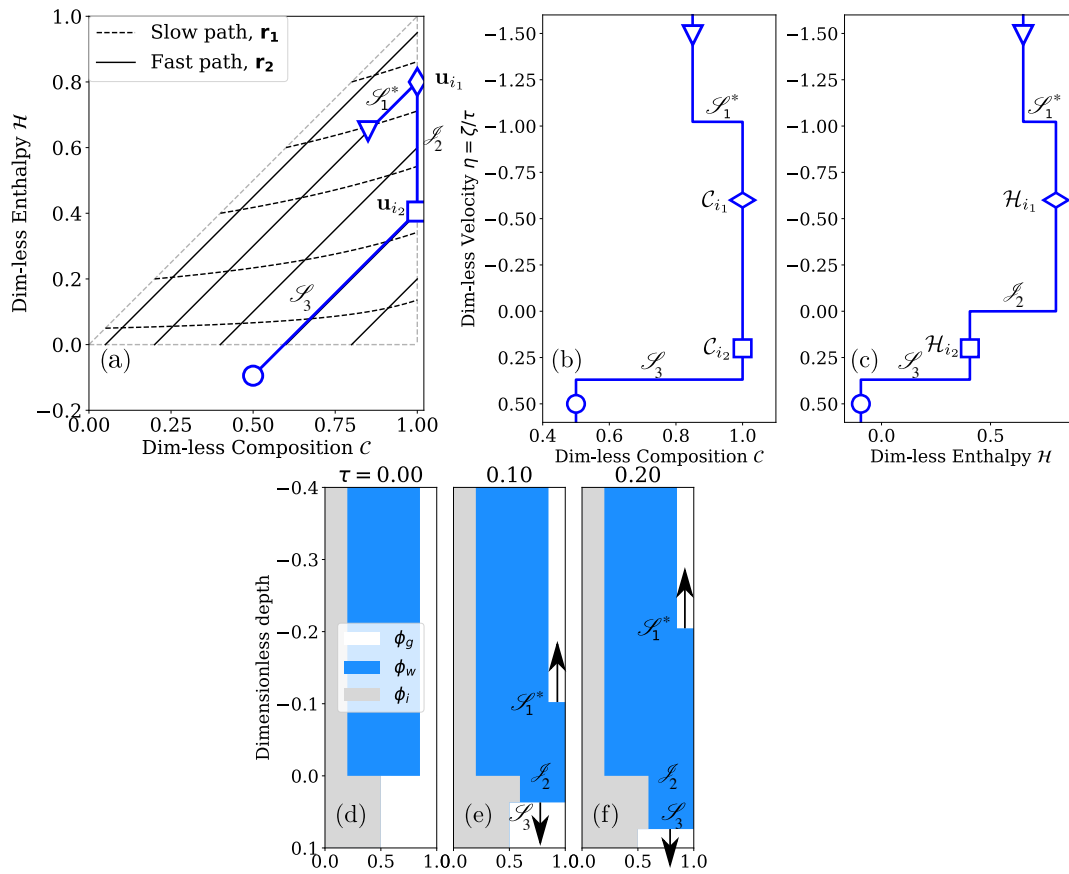


Fig. 11. Formation of a fully-saturated region when right state lies in region 1: (a) Construction of solution in the hodograph plane and their corresponding self-similar analytical solutions for (b) dimensionless composition and (c) dimensionless enthalpy with dimensionless velocity η . The result shown with dark blue line consists of a backfilling shock, \mathcal{S}_1^* , a jump, \mathcal{I}_2 , and another refreezing shock, \mathcal{S}_3 , along with two intermediate states $\mathbf{u}_{i_1} = (C_{i_1}, \mathcal{H}_{i_1})^T$ and $\mathbf{u}_{i_2} = (C_{i_2}, \mathcal{H}_{i_2})^T$. The evolution of the volume fractions of the three phases in the resulting system at dimensionless times (d) $\tau = 0$, (e) 0.1, (f) 0.2.

Figure 11 shows an example of this case where the left state corresponds to wet and temperate layer with 80% porosity (φ_l) and 65% LWC ($\phi_{w,l}$) lying on top of very cold and less porous ($T = -30^\circ\text{C}$, $\varphi_r = 50\%$) firn. This corresponds to the left and right states being $\mathbf{u}_l = (0.85, 0.65)^T$ and $\mathbf{u}_r = (0.5, -0.095)^T$. The first and second intermediate states are $\mathbf{u}_{i_1} = (1, 0.8)^T$ and $\mathbf{u}_{i_2} = (1, 0.405)^T$ respectively. The upper shock, also called a rising perched water table, is almost four times faster than the lower, refreezing front (see Figures 11*b-f*). Below the initial jump at $\zeta = 0$ the porosity is further reduced by refreezing, leading to formation of a frozen fringe (Figures 11*e-f*). The second intermediate state below jump \mathcal{J}_2 with a newly formed frozen fringe is unable to accommodate the whole volumetric flux of water, leading to the formation of a rising perched water table (see Figures 11*e-f*). Once the rising perched water table reaches the surface, it will lead to ponding and can eventually form runoff.

(iv.) 1-Backfilling shock, 2-Jump, 3-Contact discontinuity (formation of an impermeable ice layer, Case XII): This final case captures the formation of an impermeable ice layer through advection of meltwater and associated latent heat. An ice layer forms through the construction in Case XI, if the extended fast path ($\mathcal{H} = \mathcal{C} + \mathcal{C}$) emanating from the right state reach $\mathcal{C} \geq 1$ at the solidus ($\mathcal{H} = 0$) or the porosity of the second intermediate state reaches 0. This case is entirely governed by the right state and an ice layer will form if and only if the right state satisfies

$$1 - \mathcal{C}_r + \mathcal{H}_r \leq 0. \quad (71)$$

The exact location of the right state does not matter if it lies in the region of ice layer formation (grey region in Figure 12*a*). In other words, an impermeable ice layer via heat advection will form if and only if the cold content of the firn exceeds the latent enthalpy of incoming meltwater. The mathematical condition (71) in dimensional form has been given in Humphrey and others (2021b) for distinct densities of ice and water. In this limit, the solution for Case XI breaks down due to the formation of an impermeable ice layer. Figure 12 shows the region of ice layer formation which requires either very low firn porosity or temperatures in the right state. The final solution for this case is a backfilling shock, \mathcal{S}_1^* to the intermediate saturated region i_1 . The first saturated region is connected to the second intermediate state i_2 through the jump \mathcal{J}_2 . The second intermediate state i_2 is the infinitesimally thin ice layer (see Figures 12*e-f*) which blocks the further meltwater. The solution in this case can be written as

$$\mathbf{u}_l \xrightarrow{\mathcal{S}_1^*} \mathbf{u}_{i_1} \xrightarrow{\mathcal{S}_2} \mathbf{u}_{i_2} \xrightarrow{\mathcal{S}_3} \mathbf{u}_r$$

where the state solution is quantified as

$$\mathbf{u} = \begin{cases} \mathbf{u}_l, & \zeta < \Lambda_{\mathcal{S}_1^*} \\ \mathbf{u}_{i_1} = \begin{bmatrix} 1 \\ 1 - \mathcal{C}_l + \mathcal{H}_l \end{bmatrix}, & \Lambda_{\mathcal{S}_1^*} < \zeta/\tau < 0 \\ \mathbf{u}_{i_2} = \begin{bmatrix} 1 \\ 0 \end{bmatrix}, & 0 < \zeta < d\zeta \\ \mathbf{u}_r, & \zeta > d\zeta \end{cases}, \tag{72}$$

where $d\zeta$ is the infinitesimally small thickness of the ice layer.

In this case, only a single shock moves upwards similar to the filling of a bucket. The flux in the saturated region is simply zero from the mass balance at the ice layer, i.e., $q_s = f(\mathbf{u}_{i_1}) = f(\mathbf{u}_{i_2}) = 0$. The speed of the rising perched water table (first shock \mathcal{S}_1^*) is then

$$\Lambda_{\mathcal{S}_1^*}(\mathbf{u}_l) = \frac{d\zeta_U}{d\tau} = \frac{f(\mathbf{u}_l)}{\mathcal{C}_l - 1} = \frac{\mathcal{H}^n(1 - \mathcal{C}_l + \mathcal{H}_l)^{(m-n)}}{\mathcal{C}_l - 1} \tag{73}$$

which depends only on the left-state variables.

It can be deduced that either a cold firn (lower \mathcal{H}) or a nearly non-porous firn with \mathcal{C} close to unity will induce the formation of an impermeable ice layer via refreezing caused by heat advection. For example, Figure 12 shows such a solution when a wet and temperate layer of 70% porosity and 65% LWC lies on top of a cold layer with 5% porosity at $T = -30^\circ\text{C}$. These conditions correspond to $\mathbf{u}_l = (0.95, 0.65)^T$ and $\mathbf{u}_r = (0.95, -0.180)^T$ (Figures 12a-c). Here the intermediate states lie at $\mathbf{u}_{i_1} = (1, 0.7)^T$ and $\mathbf{u}_{i_2} = (1, 0)^T$ respectively. An impermeable ice layer forms as a result (see Figures 12e-f) that blocks the flow of meltwater downwards. Since there is no meltwater percolating in the lower layer, the backfilling occurs very rapidly.

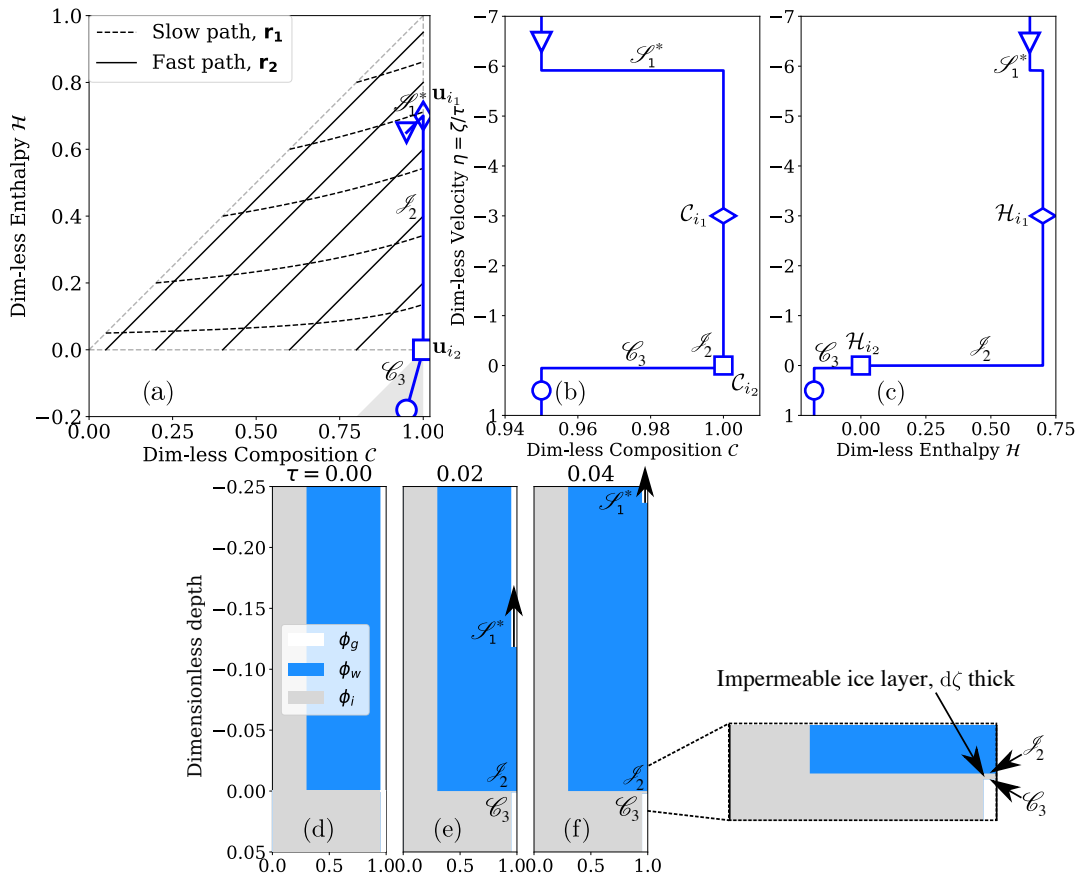


Fig. 12. Impermeable ice layer formation: (a) Construction of solution in the hodograph plane and their corresponding self-similar analytical solutions for (b) dimensionless composition and (c) dimensionless enthalpy with dimensionless velocity η . The result shown with dark blue line consists of a backfilling shock, \mathcal{S}_1^* , a jump, \mathcal{J}_2 and a contact discontinuity, \mathcal{C}_3 along with two intermediate states $\mathbf{u}_{i_1} = (c_{i_1}, \mathcal{H}_{i_1})^T$ and $\mathbf{u}_{i_2} = (c_{i_2}, \mathcal{H}_{i_2})^T$. The second intermediate state \mathbf{u}_{i_2} corresponds to the impermeable ice layer. The grey region corresponds to $1 - c + \mathcal{H} \leq 0$ where the right state resides to cause impermeable ice layer formation. The evolution of the volume fractions of the three phases in the resulting system at dimensionless times (d) $\tau = 0$, (e) 0.02, (f) 0.04.

Table 2. Summary of all analytic solutions presented in this paper along with related works that either studied or observed the corresponding scenario.

Case	Region		State properties	Solution		Physical relevance	Related work(s)	
	\mathbf{u}_l	\mathbf{u}_r		Summary	Equation(s)			Construction figure
I	2	2	$f(\mathbf{u}_l) = f(\mathbf{u}_r) \Leftrightarrow \mathbf{u}_l, \mathbf{u}_r$ connected by slow path	$\mathbf{u}_l \xrightarrow{\mathcal{C}} \mathbf{u}_r$	38, 40, 41	6 (green line)	Steady meltwater flux inside a temperate firm with a jump in porosity.	–
II	2	2	$f(\mathbf{u}_l) < f(\mathbf{u}_r)$; $\mathbf{u}_l, \mathbf{u}_r$ connected by fast path; $C_l < C_r$	$\mathbf{u}_l \xrightarrow{\mathcal{C}} \mathbf{u}_r$	39, 45	6 (blue line)	A sudden decrease in meltwater flux inside a temperate firm with constant porosity.	Colbeck (1976); Singh (1997); Clark and others (2017)
III	2	2	$f(\mathbf{u}_l) > f(\mathbf{u}_r)$; $\mathbf{u}_l, \mathbf{u}_r$ connected by fast path; $C_l > C_r$	$\mathbf{u}_l \xrightarrow{\mathcal{C}} \mathbf{u}_r$	39, 46, 47	6 (red line)	A sudden increase in meltwater flux inside a temperate firm with constant porosity.	Colbeck (1971, 1972); Singh (1997); Samimi and others (2021)
IV	2	2	$f(\mathbf{u}_l) < f(\mathbf{u}_r)$; $\mathbf{u}_l, \mathbf{u}_r$ cannot be connected by either paths; $C_l < 1$	$\mathbf{u}_l \xrightarrow{\mathcal{C}_1} \mathbf{u}_i \xrightarrow{\mathcal{C}_2} \mathbf{u}_r$	49, 51	7 (blue line)	A sudden decrease in meltwater flux inside a temperate firm with a step change in porosity.	–
V	2	2	$f(\mathbf{u}_l) > f(\mathbf{u}_r)$; $\mathbf{u}_l, \mathbf{u}_r$ cannot be connected by either paths; $C_l < 1$	$\mathbf{u}_l \xrightarrow{\mathcal{C}_1} \mathbf{u}_i \xrightarrow{\mathcal{C}_2} \mathbf{u}_r$	52, 53, 46	7 (red line)	A sudden increase in meltwater flux inside a temperate firm with a step change in porosity.	–
VI	2	2	$f(\mathbf{u}_l) > f(\mathbf{u}_r)$; $\mathbf{u}_l, \mathbf{u}_r$ cannot be connected by the combination of two paths in Region 2; slow path emanating from \mathbf{u}_l does not intersect with fast path emanating from \mathbf{u}_r , where $C < 1$	$\mathbf{u}_l \xrightarrow{\mathcal{C}_1^*} \mathbf{u}_i \xrightarrow{\mathcal{C}_2} \mathbf{u}_r$	55, 57, 58, 59, 61, 62, 63	8	A sudden increase in meltwater flux inside a temperate firm with a step decline in porosity with depth leading to formation of a rising perched water table.	Shadab and Hesse (2022)
VII	1	1	$f(\mathbf{u}_l) = f(\mathbf{u}_r) = 0$	$\mathbf{u}_l \xrightarrow{\mathcal{C}} \mathbf{u}_r$	64	9 (blue line)	A cold firm with a step change in porosity with no meltwater flux.	–
VIII	1	2	–	$\mathbf{u}_l \xrightarrow{\mathcal{C}_1} \mathbf{u}_i \xrightarrow{\mathcal{C}_2} \mathbf{u}_r$	51, 65, 66	9 (red line)	A cold firm with no meltwater flux overlying a wet, temperate firm.	–
IX	2	1	$\mathbf{u}_l, \mathbf{u}_r$ connected by extended fast path	$\mathbf{u}_l \xrightarrow{\mathcal{C}} \mathbf{u}_r$	46, 47, 67	10 (blue line)	A sudden increase in meltwater flux into a cold firm with constant porosity leading to the formation of frozen fringe.	Colbeck (1976); Clark and others (2017); Meyer and Hewitt (2017)
X	2	1	$\mathbf{u}_l, \mathbf{u}_r$ cannot be connected by extended fast path, $C_l < 1$	$\mathbf{u}_l \xrightarrow{\mathcal{C}_1} \mathbf{u}_i \xrightarrow{\mathcal{C}_2} \mathbf{u}_r$	53, 68, 69	10 (red line)	A sudden increase in meltwater flux into a cold firm with a step change porosity leading to the formation of frozen fringe.	Colbeck (1976); Clark and others (2017); Meyer and Hewitt (2017)
XI	2	1	$\mathbf{u}_l, \mathbf{u}_r$ cannot be connected by extended fast path; slow path from \mathbf{u}_l does not intersect with extended fast path from \mathbf{u}_r where $C < 1$	$\mathbf{u}_l \xrightarrow{\mathcal{C}_1^*} \mathbf{u}_i \xrightarrow{\mathcal{C}_2} \mathbf{u}_r$	55, 57, 58, 59, 60, 70, 62, 63	11	A sudden increase in meltwater flux into a cold firm with a step decrease porosity leading to the formation of frozen fringe and a rising perched water table.	Humphrey and others (2021b)
XII	2	1	\mathbf{u}_r lies in impermeable ice layer satisfying $1 - C_r - \mathcal{H}_r \leq 0$	$\mathbf{u}_l \xrightarrow{\mathcal{C}_1^*} \mathbf{u}_i \xrightarrow{\mathcal{C}_2} \mathbf{u}_r$	72, 73	12	A sudden increase in meltwater flux into a cold firm with a step decrease porosity leading to the formation an impermeable ice layer and a rising perched water table.	Humphrey and others (2021b)

4 COMPARISON AGAINST NUMERICAL SOLUTIONS AND LIMITATIONS OF THE THEORY

All of the analytic solutions described in Sections 3.3 and 3.4 show excellent comparison against the corresponding numerical solutions of Equations (8) and (9) in the absence of heat conduction (not shown for brevity). In this section we demonstrate the application of this theory to a more realistic multilayered firn leading to the formation of a perched firn aquifer. The analytic solutions are compared against the corresponding numerical solution without heat conduction. Finally, we summarize the potential limitations of the theory for consideration and future development.

4.1 Meltwater infiltration into a multilayered firn - Formation of a perched water table

This final test shows the infiltration into multilayered firn after a melt event combining two cases proposed in Section 3 that are summarized in Table 2 (see Figure 13a). This problem summates the commonly studied wetting front propagation in a temperate region (Case III) with the wetting front in a cold region and the formation of a perched water table (Case XI) that has not been studied in the firn literature. This problem demonstrates a delay in meltwater ponding at the surface due to a decay in both firn porosity and temperature with depth. The firn is 70% porous, dry and at 0°C, above a dimensionless depth of $\zeta = 1$ (Figures 13a). At time $\tau = 0$, the meltwater is generated at the surface ($\zeta = 0$), which keeps the liquid water content (denoted by LWC or ϕ_w) to 40% making the firn very wet at the surface, $\zeta = 0$. The analytic solution of this problem can be constructed in the $\mathcal{C} - \mathcal{H}$ hodograph plane in two parts (Figure 13b).

First, a wetting front \mathcal{S} initially propagates downwards with a constant dimensionless speed $\Lambda_{\mathcal{S}} = 0.28$, as given in Case III (Figures 13c-e, red dashed line). The dimensionless time when the initial front reaches the depth of transition $\zeta_t = 1$ to form a saturated region is $\tau_s = \frac{\zeta_t}{\Lambda_{\mathcal{S}}} = 1/0.28 = 3.57$, as shown in Case XI. Afterwards the saturated region forms due to large meltwater flux compared to the hydraulic conductivity of the second intermediate region formed due to refreezing below the jump $\zeta > 1$, making the flow pressure driven instead and enforcing $q_s(\tau) \leq K_{i_2}$. This saturated region expands in both directions as a perched water table (upper shock shown by green dashed line in Figure 13) rising to the surface and the wetting front \mathcal{S}_3 that percolates in the cold region (lower shock shown with blue dashed line) while refreezing a part of meltwater to warm the surrounding firn. Thus, it shows a reduction in porosity from 30% to 21.2% for $\zeta > 1$ behind the wetting front \mathcal{S}_3 at $\tau > \tau_s$ (Figure 13c). The perched water table \mathcal{S}_1^* rises upwards with

constant dimensionless velocity $\Lambda_{\mathcal{S}_1^*} = -0.268$ until ponding occurs. Meanwhile, the wetting front keeps percolating in the cold firn with reduced velocity $\Lambda_{\mathcal{S}_3} = 0.105$. Lastly, the ponding starts at a time when the rising perched water table reaches the surface so the dimensionless ponding time can be calculated theoretically as $\tau_p = \zeta_t/\Lambda_{\mathcal{S}} + (-\zeta_t)/\Lambda_{\mathcal{S}_1^*} = 1/0.28 + (-1)/(-0.268) = 7.30$. All of these dimensionless shock speeds and times are computed analytically and the resulting locations are graphed with dashed lines in Figures 13*c-e*.

These theoretical results show an excellent comparison with the numerical solutions shown in contour plots. The numerical solutions are obtained by solving the governing model (26) performed in the absence of capillary effects in between water and gas phases as well as heat conduction along with the treatment in the saturated region given by Shadab and Hesse (2024) and implementation of the enthalpy method in Shadab and others (2024a). Further, the densities of the water and the ice phases are assumed to be the same. The computational domain $\zeta \in [0, 2]$ is divided uniformly into 400 cells. The boundary condition at the top surface ($\zeta = 0$) is prescribed as the "Top condition" in Figure 13*a* whereas the bottom boundary condition is not required. This problem constitutes a very specific benchmark test for firn hydrology simulators that are able to simulate variably saturated flows. It shows how vertical heterogeneity in firn may lead to formation of perched aquifers that can cause ponding at a later stage. It also illustrates that an impermeable layer is not required to cause meltwater perching and subsequently, ponding.

4.2 Limitations of the present theory and further work

The unified kinematic wave theory makes necessary hydrologic and thermodynamic simplifications to make the system hyperbolic and amenable to solution using the method of characteristics. Some of these simplifications can be relaxed, but doing so will make the solutions more involved. On the hydrologic side, the theory neglects capillary forces in unsaturated firn, which may introduce significant errors at small spatial scales and grain sizes. Thus, it assumes that meltwater advection occurs faster as a wavefront than through diffusion via capillary suction. Capillary forces account for less than 10% of the total force, including gravity, when the meltwater flux is 10^{-8} m/s, although the percentage rapidly increases for smaller fluxes (Colbeck, 1974b). The theory assumes that the density of water and ice are the same, which underestimates the porosity reduction due to refreezing when a wetting front percolates into a cold, dry firn. The kinematic model could easily be extended to account for different densities. The present model does not assume compaction of ice due to factors such as overburden, temperature, time, and initial snow

properties (e.g., crystal shape, packing geometry), which is present in both wet and dry firn (Bader, 1954; Mellor, 1977; Herron and Langway, 1980; Amory and others, 2024). Lastly, the present theory assumes a one-dimensional flow in the direction of gravity with piecewise homogeneous firn, and does not consider preferential flow which might enhance the speed and depth of meltwater percolation at higher melt fluxes (Wever and others (2016); Vandecrux and others (2020); Jones and others (2024)).

On the thermodynamic side, the present theory assumes local thermodynamic equilibrium, which may not be a suitable assumption for rapid infiltration. Further, the theory neglects heat conduction, which may be dominant at smaller spatial scales and meltwater fluxes. Heat conduction leads to the formation of a conductive boundary layer ahead of the wetting front (Shadab and others, 2024a). The width of the thermal boundary layer is controlled by the Peclet number for enthalpy transport, as defined in Section 2.4. A high Peclet number typically leads to a thinner thermal boundary layer, indicating the dominance of heat advection over heat conduction.

However, the kinematic theory could be extended to incorporate several additional physical processes. It could be extended to account for hysteresis in relative permeabilities, which allows melt to enter dry snow without having to overcome a saturation threshold but to leave behind residual melt during drying. The method of characteristics can also be applied to study the kinematics of non-equilibrium processes, though the solutions are no longer self-similar. This could be used to analyze percolation of melt that is not in thermal equilibrium with the ice or the coarsening of ice grains due to interaction with melt. The theory could be extended to add tracer transport that could be used to study changes in isotopic composition of the ice or dissolved gases in the melt and their effect on the climatic record in ice cores. Finally, the theory could be extended to incorporate salt and used to study the effect of colligative melting point depression in firn processes or sea water intrusion into firn. As such, the kinematic theory is a useful tool to probe the physics of advective processes in firn and to provide benchmark analytic solutions to a range of coupled non-linear processes.

5 CONCLUSIONS

This work introduces a unified kinematic wave theory for meltwater infiltration into firn that helps construct analytic solutions in the hodograph plane. The theory neglects heat conduction and capillary forces while assuming a constant density for water and ice phases. We provide a suite of 12 cases of melt infiltration into firn, inspired by nature, and construct their analytic solutions while connecting most of the cases given

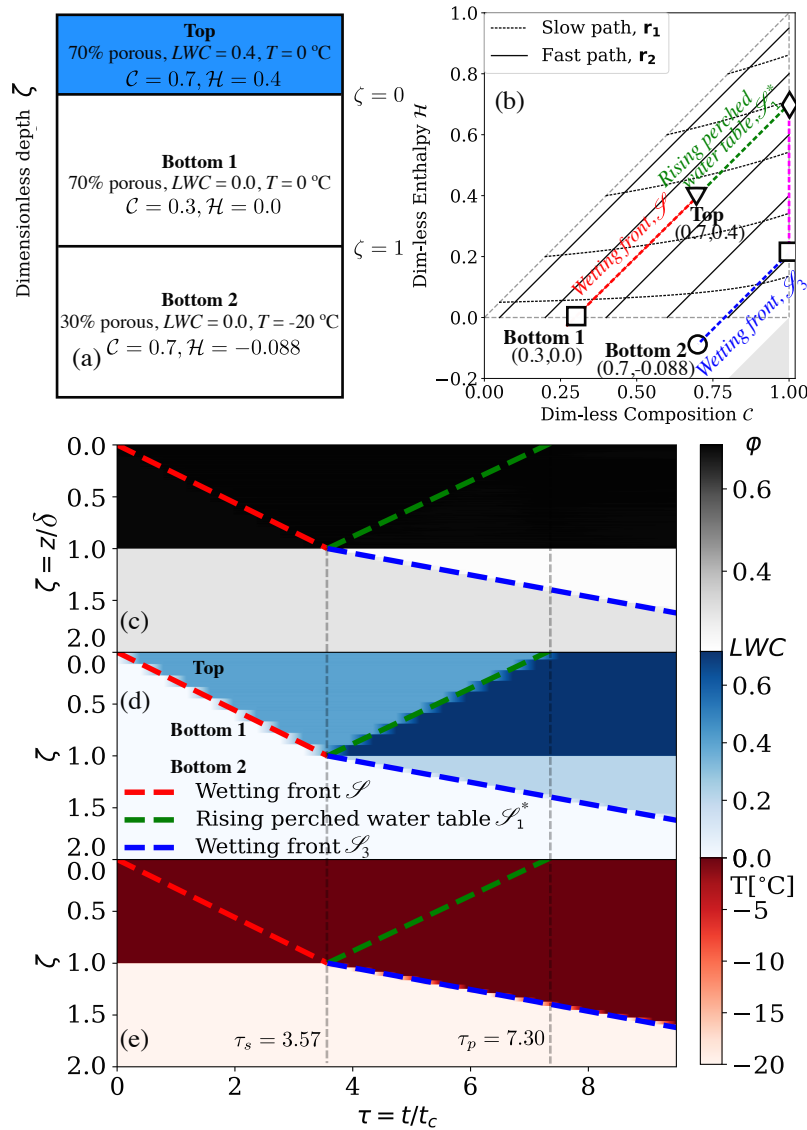


Fig. 13. Infiltration into a multilayered firm with porosity and temperature decay with depth: (a) Schematic diagram showing all of the layers (b) Construction of solution in the hodograph plane. The contours showing evolution of the firm (c) porosity ϕ , (d) liquid water content LWC or volume fraction of water ϕ_w and temperature T evaluated by the numerical simulator. Here all dashed lines show analytic solutions computed from the proposed theory. The thin, grey dashed lines show theoretically calculated dimensionless times of saturation τ_s and ponding τ_p . The theoretical evolution of the initial wetting front \mathcal{S} (red dashed line) is computed from Case III whereas the dynamics of saturated region after wetting front \mathcal{S} reaches $\zeta = 1$ shown by blue and green dashed lines is computed by Case XI. Here δ and $t_c = \delta/K_h$ are characteristic times with former being calculated from their definition 15. For example, the characteristic depth is $\delta = 5$ m and for $K_h = 5 \cdot 10^{-4}$ m/s (see Table 1), the characteristic time comes out to be $t_c = 2.53$ hours. The dimensionless wetting front speeds can be redimensionalized by multiplying with saturated (and no-matrix) hydraulic conductivity K_h .

in the literature. The previous works were predominantly limited to unsaturated wetting fronts in cold and temperate firn. We consider cases that have not been studied previously such as the formation of a perched water table (Case VI and Case XI) and the formation of an impermeable ice layer (Case XII). The simple cases discussed here can be combined to study more realistic problems, as was demonstrated for the case of infiltration into multilayered firn. The combined solutions can help construct time-varying solutions with more complexity such as variable surface conditions. There are several consequences of this work. First, one can interpret the physics of the meltwater infiltration into firn without running expensive numerical simulations. This can be used to better constrain the process of firn densification, and the partitioning of meltwater runoff versus storage, which is crucial when deriving surface mass balance. Second, these analytic solutions can help in developing better, cost-effective physics-based firn hydrological models which can then be integrated with ice-sheet and Earth system models. Further, these problems can serve as a benchmark for the next generation of wet firn hydrological models which currently show significant deviation due to a lack of benchmark problems. This comprehensive framework can significantly enhance our understanding of wet firn hydrology, a component that has been poorly understood, ultimately aiding in constraining its contribution to surface mass balance loss from glaciers and, consequently, sea-level rise.

6 ACKNOWLEDGEMENTS AND FUNDING

Support for this work was provided through NASA under Emerging World Grant number NASA 18–EW18_2–0027 and the University of Texas Institute for Geophysics under the Blue Sky Student Fellowship. The authors would like to acknowledge Dr. Surendra Adhikari and Dr. Andreas Colliander for the discussions on meltwater infiltration at the Dye-2 site in Southwest Greenland. The code and data used to generate all figures of this paper is available in a permanent repository (<https://doi.org/10.5281/zenodo.13936153>) (Shadab and others, 2024b) as well as Github for reproducibility (<https://github.com/mashadab/unified-kinematic-wave-theory>). More information is provided in the Readme of the repository.

REFERENCES

- Alexiades V and Solomon A (1993) *Mathematical Modeling of Melting and Freezing Processes*. Routledge, New York, ISBN 9780203749449 (doi: 10.1201/9780203749449)
- Amory C, Buizert C, Buzzard S, Case E, Clerx N, Culberg R, Datta R, Dey R, Drews R, Dunmire D, Eayrs C,

- Hansen N, Humbert A, Kaitheri A, Keegan K, Kuipers Munneke P, Lenaerts J, Lhermitte S, Mair D, McDowell I, Mejia J, Meyer C, Morris E, Moser D, Oraschewski F, Pearce E, de Roda Husman S, Schlegel NJ, Schultz T, Simonsen S, Stevens C, Thomas E, Thompson-Munson M, Wever N and Wouters B (2024) Firm on ice sheets. *Nature Reviews Earth & Environment*, ISSN 2662-138X (doi: 10.1038/s43017-023-00507-9)
- Anderson GM and Crerar DA (1993) *Thermodynamics in Geochemistry*. Oxford University Press, USA
- Aschwanden A, Bueler E, Khroulev C and Blatter H (2012) An enthalpy formulation for glaciers and ice sheets. *Journal of Glaciology*, **58**(209), 441–457 (doi: 10.3189/2012JoG11J088)
- Bader H (1954) Sorges law of densification of snow on high polar glaciers. *Journal of Glaciology*, **2**(15), 319–323 (doi: 10.3189/S0022143000025144)
- Bartelt P and Lehning M (2002) A physical SNOWPACK model for the Swiss avalanche warning. *Cold Regions Science and Technology*, **35**(3), 123–145, ISSN 0165232X (doi: 10.1016/S0165-232X(02)00074-5)
- Bear J (2013) *Dynamics of Fluids in Porous Media*. Courier Corporation
- Bell RE, Banwell AF, Trusel LD and Kingslake J (2018) Antarctic surface hydrology and impacts on ice-sheet mass balance. *Nature Climate Change*, **8**(12), 1044–1052, ISSN 17586798 (doi: 10.1038/s41558-018-0326-3)
- Blunt MJ (2017) *Multiphase Flow in Permeable Media: A Pore-scale Perspective*. Cambridge University Press
- Brooks R and Corey A (1964) Hydraulic properties of porous media - hydrology paper no. 3. *Civil Engineering Department, Colorado State University, Fort Collins, CO*
- Carlson FM (1981) Simulation of relative permeability hysteresis to the nonwetting phase. In *SPE Annual Technical Conference and Exhibition?*, SPE-10157, SPE (doi: 10.2118/10157-MS)
- Carman PC (1937) Fluid flow through granular beds. *Trans. Inst. Chem. Eng.*, **15**, 150–166
- Carnahan E, Wolfenbarger N, Jordan J and Hesse M (2021) New insights into temperature-dependent ice properties and their effect on ice shell convection for icy ocean worlds. *Earth and Planetary Science Letters*, **563**(116886), ISSN 0012821X (doi: 10.1016/j.epsl.2021.116886)
- Clark M, Nijssen B and Luce C (2017) An analytical test case for snow models. *Water Resources Research*, **53**(1), 909–922, ISSN 0043-1397 (doi: 10.1002/2016WR019672)
- Colbeck S (1972) A theory of water percolation in snow. *Journal of Glaciology*, **11**(63), 369–385 (doi: 10.3189/S0022143000022346)
- Colbeck S (1974a) Water flow through snow overlying an impermeable boundary. *Water Resources Research*, **10**(1), 119–123 (doi: 10.1029/WR010i001p00119)

- Colbeck S (1991) The layered character of snow covers. *Reviews of Geophysics*, **29**(1), 81–96, ISSN 8755-1209 (doi: 10.1029/90RG02351)
- Colbeck S and Anderson EA (1982) The permeability of a melting snow cover. *Water Resources Research*, **18**(4), 904–908 (doi: 10.1029/WR018i004p00904)
- Colbeck SC (1971) One-dimensional water flow through snow. *Cold Regions Research and Engineering Laboratory (US)*
- Colbeck SC (1974b) The capillary effects on water percolation in homogeneous snow. *Journal of Glaciology*, **13**(67), 85–97 (doi: 10.3189/S002214300002339X)
- Colbeck SC (1976) An analysis of water flow in dry snow. *Water Resources Research*, **12**(3), 523–527 (doi: 10.1029/WR012i003p00523)
- Colbeck SC (1979) Water flow through heterogeneous snow. *Cold Regions Science and Technology*, **1**(1), 37–45 (doi: 10.1016/0165-232X(79)90017-X)
- Colbeck SC and Davidson G (1973) Water percolation through homogeneous snow. *IAHS publ*, **107**(1), 242–257
- Coléou C and Lesaffre B (1998) Irreducible water saturation in snow: experimental results in a cold laboratory. *Annals of Glaciology*, **26**, 64–68 (doi: 10.3189/1998AoG26-1-64-68)
- Colliander A, Mousavi M, Marshall S, Samimi S, Kimball JS, Miller JZ, Johnson J and Burgin M (2022) Ice sheet surface and subsurface melt water discrimination using multi-frequency microwave radiometry. *Geophysical Research Letters*, **49**(4), e2021GL096599 (doi: 10.1029/2021GL096599)
- Cueto-Felgueroso L and Juanes R (2008) Nonlocal interface dynamics and pattern formation in gravity-driven unsaturated flow through porous media. *Physical Review Letters*, **101**(24), ISSN 00319007 (doi: 10.1103/PhysRevLett.101.244504)
- Cuffey KM and Paterson WSB (2010) *The Physics of Glaciers*. Academic Press
- de la Peña S, Howat IM, Nienow PW, van den Broeke MR, Mosley-Thompson E, Price SF, Mair D, Noël B and Sole AJ (2015) Changes in the firn structure of the western Greenland Ice Sheet caused by recent warming. *The Cryosphere*, **9**(3), 1203–1211, ISSN 1994-0424 (doi: 10.5194/tc-9-1203-2015)
- Forster RR, Box JE, Van Den Broeke MR, Miège C, Burgess EW, Van Angelen JH, Lenaerts JT, Koenig LS, Paden J, Lewis C and others (2014) Extensive liquid meltwater storage in firn within the greenland ice sheet. *Nature Geoscience*, **7**(2), 95–98 (doi: 10.1038/ngeo2043)

- Ghaderi Zefreh M, Doster F and Hesse MA (2019) Theory of dissolution and precipitation waves redux. *AICHE Journal*, **65**(6), e16573 (doi: 10.1002/aic.16573)
- Harper J, Humphrey N, Pfeffer WT, Brown J and Fettweis X (2012) Greenland ice-sheet contribution to sea-level rise buffered by meltwater storage in firn. *Nature*, **491**(7423), 240–3, ISSN 1476-4687 (doi: 10.1038/nature11566)
- Harper J, Saito J and Humphrey N (2023) Cold season rain event has impact on greenland's firn layer comparable to entire summer melt season. *Geophysical Research Letters*, **50**(14), e2023GL103654 (doi: 10.1029/2023GL103654)
- Hassanizadeh S, Celia M and Dahle H (2002) Dynamic effect in the capillary pressure saturation relationship and its impacts on unsaturated flow. *Vadose Zone Journal*, **1**(1), 38–57, ISSN 1539-1663 (doi: 10.2136/vzj2002.3800)
- Heilig A, Eisen O, MacFerrin M, Tedesco M and Fettweis X (2018) Seasonal monitoring of melt and accumulation within the deep percolation zone of the greenland ice sheet and comparison with simulations of regional climate modeling. *The Cryosphere*, **12**(6), 1851–1866 (doi: 10.5194/tc-12-1851-2018)
- Herron MM and Langway CC (1980) Firn densification: an empirical model. *Journal of Glaciology*, **25**(93), 373–385 (doi: 10.3189/S0022143000015239)
- Hirashima H, Yamaguchi S and Katsushima T (2014) A multi-dimensional water transport model to reproduce preferential flow in the snowpack. *Cold Regions Science and Technology*, **108**, 80–90, ISSN 0165232X (doi: 10.1016/j.coldregions.2014.09.004)
- Humphrey N, Harper J and Meierbachtol T (2021a) Physical limits to meltwater penetration in firn. *Journal of Glaciology*, **67**(265), 952–960, ISSN 0022-1430 (doi: 10.1017/jog.2021.44)
- Humphrey NF, Harper JT and Pfeffer WT (2012) Thermal tracking of meltwater retention in greenland's accumulation area. *Journal of Geophysical Research: Earth Surface*, **117**(F1) (doi: 10.1029/2011JF002083)
- Humphrey NF, Harper JT and Meierbachtol TW (2021b) Physical limits to meltwater penetration in firn. *Journal of Glaciology*, **67**(265), 952–960 (doi: 10.1017/jog.2021.44)
- Illangasekare T, Walter R, Meier M and Pfeffer WT (1990) Modeling of meltwater infiltration in subfreezing snow. *Water Resources Research*, **26**(5), 1001–1012, ISSN 19447973 (doi: 10.1029/WR026i005p01001)
- Jones ND, Moure A and Fu X (2024) Pattern formation of freezing infiltration in porous media. *Physical Review Fluids*, **9**(12), 123802 (doi: 10.1103/PhysRevFluids.9.123802)
- Jordan JS and Hesse MA (2015) Reactive transport in a partially molten system with binary solid solution. *Geochemistry, Geophysics, Geosystems*, **16**(12), 4153–4177 (doi: 10.1002/2015GC005956)

- Jordan R (1991) A One-Dimensional Temperature Model for a Snow Cover. Technical report, U.S. Army Corps of Engineers, Cold Regions Research and Engineering Laboratory, Special Report 91-16
- Katsushima T, Yamaguchi S, Kumakura T and Sato A (2013) Experimental analysis of preferential flow in dry snowpack. *Cold Regions Science and Technology*, **85**, 206–216, ISSN 0165232X (doi: 10.1016/j.coldregions.2012.09.012)
- Knight CA (1971) Experiments on the contact angle of water on ice. *Philosophical magazine*, **23**(181), 153–165 (doi: 10.1080/14786437108216369)
- Kozeny J (1927) Über kapillare leitung der wasser in boden. *Royal Academy of Science, Vienna, Proc. Class I*, **136**, 271–306
- Kuipers Munneke P, Ligtenberg SR, Suder EA and Van Den Broeke MR (2015) A model study of the response of dry and wet firn to climate change. *Annals of Glaciology*, **56**(70), 1–8, ISSN 02603055 (doi: 10.3189/2015AoG70A994)
- Leroux N and Pomeroy J (2017) Modelling capillary hysteresis effects on preferential flow through melting and cold layered snowpacks. *Advances in Water Resources*, **107**, 250–264, ISSN 03091708 (doi: 10.1016/j.advwatres.2017.06.024)
- Leroux N and Pomeroy J (2019) Simulation of capillary pressure overshoot in snow combining trapping of the wetting phase with a nonequilibrium Richards equation model. *Water Resources Research*, **55**(1), 236–248, ISSN 19447973 (doi: 10.1029/2018WR022969)
- LeVeque RJ (1992) *Numerical Methods for Conservation Laws*, volume 132. Springer (doi: 10.1007/978-3-0348-5116-9)
- Lighthill MJ and Whitham GB (1955) On kinematic waves ii. a theory of traffic flow on long crowded roads. *Proceedings of the Royal Society of London. Series A. Mathematical and Physical Sciences*, **229**(1178), 317–345
- Ligtenberg S, Helsen M and van den Broeke M (2011) An improved semi-empirical model for the densification of Antarctic firn. *The Cryosphere*, **5**(4), 809–819, ISSN 1994-0424 (doi: 10.5194/tc-5-809-2011)
- Marsh P and Woo M (1984) Wetting front advance and freezing of meltwater within a snow cover: 1. Observations in the Canadian Arctic. *Water Resources Research*, **20**(12), 1853–1864, ISSN 0043-1397 (doi: 10.1029/WR020i012p01853)
- Mellor M (1977) Engineering properties of snow. *Journal of Glaciology*, **19**(81), 15–66 (doi: 10.3189/S002214300002921X)
- Meyer CR and Hewitt IJ (2017) A continuum model for meltwater flow through compacting snow. *The Cryosphere*, **11**(6), 2799–2813 (doi: 10.5194/tc-11-2799-2017)

- Moure A, Jones N, Pawlak J, Meyer C and Fu X (2023) A thermodynamic nonequilibrium model for preferential infiltration and refreezing of melt in snow. *Water Resources Research*, **59**(5), ISSN 19447973 (doi: 10.1029/2022WR034035)
- Noël B, Van De Berg WJ, Lhermitte S, Wouters B, Machguth H, Howat I, Citterio M, Moholdt G, Lenaerts JT and Van Den Broeke MR (2017) A tipping point in refreezing accelerates mass loss of Greenland's glaciers and ice caps. *Nature Communications*, **8**(1), 1–8, ISSN 20411723 (doi: 10.1038/ncomms14730)
- Noël B, Lenaerts JT, Lipscomb WH, Thayer-Calder K and van den Broeke MR (2022) Peak refreezing in the Greenland firn layer under future warming scenarios. *Nature Communications*, **13**(1), ISSN 20411723 (doi: 10.1038/s41467-022-34524-x)
- Pfeffer WT and Humphrey NF (1998) Formation of ice layers by infiltration and refreezing of meltwater. *Annals of Glaciology*, **26**, 83–91, ISSN 0260-3055 (doi: 10.3189/1998AoG26-1-83-91)
- Pfeffer WT, Meier MF and Illangasekare TH (1991) Retention of Greenland runoff by refreezing: implications for projected future sea level change. *Journal of Geophysical Research*, **96**(C12), ISSN 01480227 (doi: 10.1029/91jc02502)
- Samimi S, Marshall SJ and MacFerrin M (2020) Meltwater penetration through temperate ice layers in the percolation zone at dye-2, greenland ice sheet. *Geophysical Research Letters*, **47**(15), e2020GL089211 (doi: 10.1029/2020GL089211)
- Samimi S, Marshall SJ, Vandecrux B and MacFerrin M (2021) Time-domain reflectometry measurements and modeling of firn meltwater infiltration at dye-2, greenland. *Journal of Geophysical Research: Earth Surface*, **126**(10), e2021JF006295 (doi: 10.1029/2021JF006295)
- Schneebeli M (1995) Development and stability of preferential flow paths in a layered snowpack. In *Biogeochemistry of Seasonally Snow-Covered Catchm*, 228, 89, Boulder, ISBN 0-947571-44-2, ISSN 0144-7815
- Shadab MA and Hesse MA (2022) Analysis of gravity-driven infiltration with the development of a saturated region. *Water Resources Research*, e2022WR032963 (doi: 10.1029/2022WR032963)
- Shadab MA and Hesse MA (2024) A hyperbolic-elliptic pde model and conservative numerical method for gravity-dominated variably-saturated groundwater flow. *Advances in Water Resources*, 104736 (doi: 10.1016/j.advwatres.2024.104736)
- Shadab MA, Adhikari S, Rutishauser A, Grima C and Hesse MA (2024a) A mechanism for ice layer formation in glacial firn. *Geophysical Research Letters*, **51**(15), e2024GL109893 (doi: 10.1029/2024GL109893)

- Shadab MA, Rutishauser A, Grima C and Hesse MA (2024b) unified-kinematic-wave-theory (v1.0). *Zenodo* (doi: 10.5281/zenodo.13936153)
- Sharp R (1951) Meltwater behavior in firn on upper seaward glacier, st. elias mountains, canada. *IASH Publ.*, **32**, 246–253
- Singh V, Bengtsson L and Westerstrom G (1997) Kinematic wave modelling of vertical movement of snowmelt water through a snowpack. *Hydrological Processes*, **11**(2), 149–167, ISSN 08856087 (doi: 10.1002/(SICI)1099-1085(199702)11:2<149::AID-HYP427>3.3.CO;2-F)
- Singh VP (1997) *Kinematic Wave Modeling in Water Resources: Environmental Hydrology*. John Wiley & Sons
- Smith R (1983) Approximate Soil Water Movement by Kinematic Characteristics. *Soil Science Society of America Journal*, **47**(1), 3–8, ISSN 03615995 (doi: 10.2136/sssaj1983.03615995004700010001x)
- Stevens C, Verjans V, Lundin J, Kahle E, Horlings A, Horlings B and Waddington E (2020) The Community Firn Model (CFM) v1.0. *Geoscientific Model Development*, **13**(9), 4355–4377, ISSN 1991-9603 (doi: 10.5194/gmd-13-4355-2020)
- Tek M (1957) Development of a generalized darcy equation. *Journal of Petroleum Technology*, **9**(06), 45–47
- Van Angelen JH, Lenaerts JT, Van Den Broeke MR, Fettweis X and Van Meijgaard E (2013) Rapid loss of firn pore space accelerates 21st century Greenland mass loss. *Geophysical Research Letters*, **40**(10), 2109–2113, ISSN 00948276 (doi: 10.1002/grl.50490)
- Vandecrux B, Mottram R, Langen PL, Fausto RS, Olesen M, Stevens CM, Verjans V, Leeson A, Ligtenberg S, Kuipers Munneke P and others (2020) The firn meltwater retention model intercomparison project (retmip): evaluation of nine firn models at four weather station sites on the greenland ice sheet. *The Cryosphere*, **14**(11), 3785–3810 (doi: 10.5194/tc-14-3785-2020)
- Venkatraman A, Hesse MA, Lake LW and Johns RT (2014) Analytical solutions for flow in porous media with multi-component cation exchange reactions. *Water Resources Research*, **50**(7), 5831–5847 (doi: 10.1002/2013WR015091)
- Verjans V, Leeson AA, Stevens CM, MacFerrin M, Noël B and van den Broeke MR (2019) Development of physically based liquid water schemes for Greenland firn-densification models. *The Cryosphere*, **13**(7), 1819–1842, ISSN 1994-0424 (doi: 10.5194/tc-13-1819-2019)
- Verjans V, Leeson AA, McMillan M, Stevens CM, van Wessem JM, van de Berg WJ, van den Broeke MR, Kittel C, Amory C, Fettweis X, Hansen N, Boberg F and Mottram R (2021) Uncertainty in east Antarctic firn thickness constrained using a model ensemble approach. *Geophysical Research Letters*, **48**(7), ISSN 19448007 (doi: 10.1029/2020GL092060)

Vionnet V, Brun E, Morin S, Boone A, Faroux S, Le Moigne P, Martin E and Willemet JM (2012) The detailed snowpack scheme Crocus and its implementation in SURFEX v7.2. *Geoscientific Model Development*, **5**(3), 773–791, ISSN 1991-9603 (doi: 10.5194/gmd-5-773-2012)

Wever N, Fierz C, Mitterer C, Hirashima H and Lehning M (2014) Solving Richards Equation for snow improves snowpack meltwater runoff estimations in detailed multi-layer snowpack model. *The Cryosphere*, **8**(1), 257–274, ISSN 1994-0424 (doi: 10.5194/tc-8-257-2014)

Wever N, Würzer S, Fierz C and Lehning M (2016) Simulating ice layer formation under the presence of preferential flow in layered snowpacks. *Cryosphere*, **10**(6), 2731–2744, ISSN 19940424 (doi: 10.5194/tc-10-2731-2016)

A FLUX GRADIENT AND LEMMA RELATED TO EIGEN-DECOMPOSITION

The partial derivatives of the flux function given in equation (24) give:

$$f_{,\mathcal{H}} = \frac{\partial f_{\mathcal{C}}}{\partial \mathcal{H}} = \begin{cases} 0, & \mathcal{H} \leq 0 \\ \mathcal{H}^{n-1}(1 - \mathcal{C} + \mathcal{H})^{m-n-1}(n(1 - \mathcal{C}) + m\mathcal{H}), & 0 < \mathcal{H} < \mathcal{C} \end{cases} \quad (74)$$

$$f_{,\mathcal{C}} = \frac{\partial f_{\mathcal{H}}}{\partial \mathcal{C}} = \begin{cases} 0, & \mathcal{H} \leq 0 \\ -(m - n)\mathcal{H}^n(1 - \mathcal{C} + \mathcal{H})^{m-n-1}, & 0 < \mathcal{H} < \mathcal{C} \end{cases} \quad (75)$$

Lemma A.1. *Prove that λ_2 is non-negative and increases monotonically in the direction of integral curves corresponding to the second eigenvector \mathbf{r}_2 (fast paths) in the three phase region, $0 < \mathcal{H} < \mathcal{C}$.*

Proof. Since $\mathcal{H} > 0$, $-\mathcal{C} < \mathcal{H} - \mathcal{C}$, and $0 \leq \mathcal{C} < 1$,

$$\lambda_2 = n\mathcal{H}^{n-1}(1 - \mathcal{C} + \mathcal{H})^{m-n} > 0 \quad (76)$$

Along the fast path, $\mathcal{C} = \mathcal{H} + \mathfrak{C}$,

$$\lambda_2 = n\mathcal{H}^{n-1}(1 - \mathcal{C} + \mathcal{H})^{m-n} \quad (77)$$

$$= n\mathcal{H}^{n-1}(1 - (\mathcal{H} + \mathfrak{C}) + \mathcal{H})^{m-n} \quad (78)$$

$$= n\mathcal{H}^{n-1}(1 + \mathfrak{C})^{m-n} \quad (79)$$

Now, taking the derivative with respect to \mathcal{H} , we get

$$\frac{d\lambda_2}{d\mathcal{H}} = n(n-1)\mathcal{H}^{n-2}(1+\mathfrak{C})^{m-n} \quad (80)$$

As $\mathcal{H} > 0$ and $\mathfrak{C} = \mathcal{C} - \mathcal{H} < 1$ in three phase region,

$$\frac{d\lambda_2}{d\mathcal{H}} > 0, \quad \text{for } n > 1 \quad (81)$$

Therefore, λ_2 is non-negative and increases monotonically in the direction of \mathbf{r}_2 when $n > 1$. \square

Lemma A.2. *Prove that fast paths are parallel to constant porosity φ contours in three phase region, $0 < \mathcal{H} \leq \mathcal{C}$.*

Proof. In the three-phase region, the porosity $\varphi = \phi_w + \phi_g = \mathcal{H} + (1 - \mathcal{C})$. For a constant porosity $d\varphi = 0$, therefore

$$d\varphi = d(\mathcal{H} + (1 - \mathcal{C})) \quad (82)$$

$$0 = d\mathcal{H} - d\mathcal{C} \quad (83)$$

$$1 = \frac{d\mathcal{H}}{d\mathcal{C}} \quad (84)$$

$$\mathcal{C} = \mathcal{H} + \mathfrak{C} \quad (85)$$

where \mathfrak{C} again is an integration constant. Therefore, the constant porosity φ contours are the integral curves corresponding to second eigenvector \mathbf{r}_2 (fast paths) in three-phase region. \square